

Three-dimensional delayed-detonation models with nucleosynthesis for Type Ia supernovae

Ivo R. Seitenzahl^{1,2} ^{*}, Franco Ciaraldi-Schoolmann², Friedrich K. Röpke¹,
Michael Fink¹, Wolfgang Hillebrandt², Markus Kromer², Rüdiger Pakmor³,
Ashley J. Ruiter², Stuart A. Sim⁴, Stefan Taubenberger²

¹*Institut für Theoretische Physik und Astrophysik, Universität Würzburg, Emil-Fischer-Straße 31, 97074 Würzburg*

²*Max-Planck-Institut für Astrophysik, Karl-Schwarzschild-Straße 1, 85748 Garching, Germany*

³*Heidelberger Institut für Theoretische Studien, Schloss-Wolfsbrunnengasse 35, 69118 Heidelberg, Germany*

⁴*Research School of Astronomy and Astrophysics, Mount Stromlo Observatory, Cotter Road, Weston Creek, ACT 2611, Australia*

14 November 2012

ABSTRACT

We present results for a suite of fourteen three-dimensional, high resolution hydrodynamical simulations of delayed-detonation models of Type Ia supernova (SN Ia) explosions. This model suite comprises the first set of three-dimensional SN Ia simulations with detailed isotopic yield information. As such, it may serve as a database for Chandrasekhar-mass delayed-detonation model nucleosynthetic yields and for deriving synthetic observables such as spectra and light curves. We employ a physically motivated, stochastic model based on turbulent velocity fluctuations and fuel density to calculate in situ the deflagration to detonation transition (DDT) probabilities. To obtain different strengths of the deflagration phase and thereby different degrees of pre-expansion, we have chosen a sequence of initial models with 1, 3, 5, 10, 20, 40, 100, 150, 200, 300, and 1600 (two different realizations) ignition kernels in a hydrostatic white dwarf with central density of $2.9 \times 10^9 \text{ g cm}^{-3}$, plus in addition one high central density ($5.5 \times 10^9 \text{ g cm}^{-3}$) and one low central density ($1.0 \times 10^9 \text{ g cm}^{-3}$) rendition of the 100 ignition kernel configuration. For each simulation we determined detailed nucleosynthetic yields by post-processing 10^6 tracer particles with a 384 nuclide reaction network. All delayed detonation models result in explosions unbinding the white dwarf, producing a range of ^{56}Ni masses from 0.32 to $1.11 M_{\odot}$. As a general trend, the models predict that the stable neutron-rich iron group isotopes are not found at the lowest velocities, but rather at intermediate velocities ($\sim 3,000 - 10,000 \text{ km s}^{-1}$) in a shell surrounding a ^{56}Ni -rich core. The models further predict relatively low velocity oxygen and carbon, with typical minimum velocities around 4,000 and $10,000 \text{ km s}^{-1}$, respectively.

Key words: nuclear reactions, nucleosynthesis, abundances — supernovae: general — white dwarfs

1 INTRODUCTION

Type Ia supernovae (SNe Ia) play essential roles in the basic frameworks of many branches of astrophysics: In star formation and galaxy dynamics by heating cold interstellar gas (e.g. Scannapieco et al. 2008), in high energy astrophysics as sources of Galactic positrons (e.g. Chan & Lingenfelter 1993; Prantzos et al. 2011), in galactic chemical evolution by enriching the interstellar gas with α , Fe-peak, and possibly p-process elements (e.g. Timmes et al. 1995; Kobayashi & Nomoto 2009; Travaglio et al. 2011) and last but not least in cosmology as distance indicators

(e.g. Riess et al. 1998; Schmidt et al. 1998; Perlmutter et al. 1999). In spite of their ubiquitous presence in astrophysics, no progenitor systems have been observed and unambiguous identification of their nature remains elusive. Essentially by means of exclusion, white dwarf (WD) stars in interacting binary systems are the only viable proposed progenitor systems (cf. Bloom et al. 2012).

In the last few years we have witnessed revived interest of the double detonation He-accretion channel (e.g. Livne 1990; Livne & Glasner 1990; Woosley & Weaver 1994; Höflich & Khokhlov 1996; Nugent et al. 1997; Fink et al. 2007, 2010; Kromer et al. 2010; Woosley et al. 2011) and increasing support from theorists for the double degenerate channel (Gilfanov & Bogdán 2010; Pakmor et al. 2010; Pakmor et al. 2011;

^{*} email:irs@mpa-garching.mpg.de

Pakmor et al. 2012), culminating in mounting evidence that SN 2011fe was possibly due to a merger of two white dwarfs (e.g. Bloom et al. 2012; Chomiuk et al. 2012; Röpke et al. 2012). In spite of these recent developments, Chandrasekhar-mass models, which had been the favoured explosion scenario by many in the last two decades, still retain a list of strong arguments in their favor. For example, blue shifted Na-absorption features along the lines of sight towards SNe Ia are interpreted as a clear signature of the single degenerate channel (Patat et al. 2007; Sternberg et al. 2011). Further support to the single degenerate scenario is given by the fact that two recurrent nova systems are known where the accreting WD is near the Chandrasekhar-limit (RS Oph and U Sco), which tells us that potential progenitor systems do exist in nature. In fact, the supernova PTF 11kx is best described by a symbiotic nova progenitor system (Dilday et al. 2012).

The issue is further complicated by the fact that the evolution of zero-age binary systems towards potential SN Ia progenitor systems is still not well understood and remains a very active area of research today (e.g. Ruiter et al. 2009, 2011; Mennekens et al. 2010; Wang et al. 2010). Binary population simulations, in which a large number ($\gtrsim 10^6$) of binaries can be rapidly evolved from the zero-age main sequence for a Hubble time, are the only way in which one can obtain reliable estimates of relative birthrates for different progenitor scenarios. However, the physics of binary star evolution is very complex and some evolutionary phases are poorly understood (e.g., van der Sluis et al. 2010). For example, the evolution of single degenerate Chandrasekhar mass progenitors strongly relies on the assumptions made about WD mass accretion rates and retention efficiencies, for which there are differing camps of thought (cf. Prialnik & Kovetz 1995; Han & Podsiadlowski 2004). Despite the different assumptions made in various binary population codes, many of the codes do predict that single degenerate (Chandrasekhar mass) scenario progenitors are still promising candidates for at least some fraction of Type Ia supernovae (see Nelemans et al. 2012, table 1).

Near Chandrasekhar-mass explosion models in the single degenerate channel have long been considered as favorites to explain SNe Ia. The realization that a detonation burning through a near Chandrasekhar-mass white dwarf in hydrostatic equilibrium (Arnett 1969) produces mainly material that has been processed to nuclear statistical equilibrium (NSE) and not enough intermediate mass elements (IMEs), such as silicon or sulfur, has led to the introduction of “delayed detonation” models (Khokhlov 1989). The key features of delayed detonation models are the following:

- First nuclear burning is ignited in a deflagration flame producing mainly iron group elements (IGEs) in the initial burning phase at high density.
- The energy released in this sub-sonically propagating mode of nuclear burning leads to an expansion of the star, moving unburned nuclear fuel to lower density.
- After some time delay a supersonically moving mode of nuclear burning – a detonation – emerges.
- The supersonically moving detonation front quickly overruns much of the remaining fuel, a significant fraction of which only burns to IMEs owing to the reduced burning densities resulting from the pre-expansion.

Several three-dimensional models of delayed detonation Chandrasekhar-mass explosions have been published in the variants of deflagration to detonation transition (DDT) (Gamezo et al. 2005; Röpke & Niemeyer 2007; Bravo & García-Senz 2008; Seitenzahl et al. 2011; Röpke et al. 2012), gravitationally con-

fining detonation (GCD) (Jordan et al. 2008, 2012), and pulsational reverse detonation (PRD) models (Bravo & García-Senz 2009; Bravo et al. 2009). Generally, information on the chemical composition of the ejecta for these models is either not given or limited to ^{56}Ni and a coarse description of elemental yields or major nucleosynthesis groups, such as unburned carbon or oxygen, IMEs, or IGEs. The exception are Bravo et al. (2009), who show a table of 24 isotopes for two PRD explosion models. While full isotopic information of the ejecta for three-dimensional *pure deflagration* explosions exists in the literature (e.g. Travaglio et al. 2004; Röpke et al. 2006a) such detailed information for delayed detonation explosion models is currently only available for a few two-dimensional (Meakin et al. 2009; Maeda et al. 2010b) or one-dimensional explosion models (e.g. Iwamoto et al. 1999; Brachwitz et al. 2000). Here, for the first time, we present detailed nucleosynthetic yields for a suite of high resolution, three dimensional hydrodynamical explosion simulations, producing a large range of ^{56}Ni masses between ~ 0.32 and $1.11 M_{\odot}$.

In Section 2 we introduce our initial stellar models and the ignition setups, briefly describe our thermonuclear supernova hydrodynamics code LEAFS, elaborate on how we model the deflagration to detonation transition, and discuss the morphologies of the explosion models. In Section 3 we summarize how we obtain the full compositional information by post-processing of tracer particles and we present the yields for all models. In Section 4 we discuss the relevance of our contribution and conclude with an outlook.

2 HYDRODYNAMIC SIMULATIONS

2.1 Initial models

For initial stellar models we have chosen isothermal non-rotating WDs in hydrostatic equilibrium. The models have a central density of $\rho_c = 2.9 \times 10^9 \text{ g cm}^{-3}$ ($M = 1.400 M_{\odot}$, $R = 1.96 \times 10^8 \text{ cm}$), but we also include a low central density $\rho_c = 1.0 \times 10^9 \text{ g cm}^{-3}$ ($M = 1.361 M_{\odot}$, $R = 1.96 \times 10^8 \text{ cm}$) and a high central density $\rho_c = 5.5 \times 10^9 \text{ g cm}^{-3}$ ($M = 1.416 M_{\odot}$, $R = 1.96 \times 10^8 \text{ cm}$) version of the N100 model (Röpke et al. 2012). These low and high central density models are labeled N100L and N100H, respectively.

For all models we set up a cold ($T = 5 \times 10^5 \text{ K}$), hydrostatic WD for a homogeneous composition of ^{12}C and ^{16}O in equal parts by mass. To account for an assumed solar metallicity of the zero-age main-sequence progenitor, we set the electron fraction to $Y_e = 0.49886$, which corresponds to a ^{22}Ne content of 2.5 per cent by mass (see Sec 3).

The ignition of the deflagration is critical for the outcome of the explosion. This stage, however, is difficult to model. A century of convective carbon burning precedes the thermonuclear runaway. The flow field in this “simmering phase” is expected to be highly turbulent and thus hard to address numerically (but see e.g., Höflich & Stein 2002; Kuhlen et al. 2006; Zingale et al. 2009; Nonaka et al. 2012) and not finally settled. Not explicitly modeling the ignition phase, we therefore take a pragmatic approach and treat the ignition geometry as a free parameter. This has two aspects: (i) the ignition shape has to seed unstable modes in a realistic way and (ii) it should capture the correct position of the ignition region relative to the WD’s center. Regarding (i), we chose to ignite the deflagration in a number of spherical sparks near the center of the WD. Although recent simulations suggest that a high number of nearly simultaneous ignitions appears unlikely (Nonaka et al.

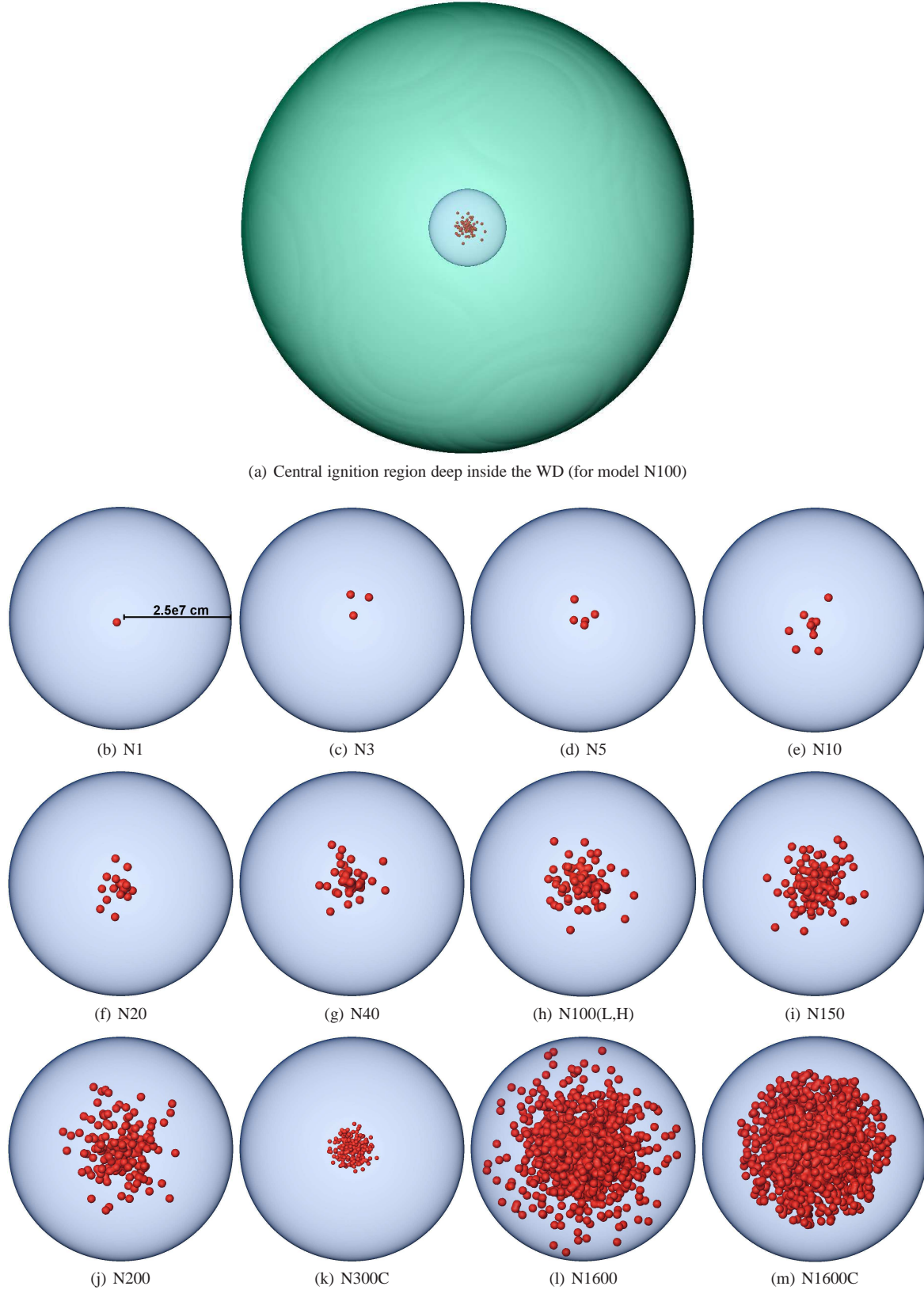


Figure 1. Ignition geometries of the deflagration for all models. We show the arranged ignition kernels (red spheres) and a transparent blue contour where the distance to the center is 2.5×10^7 cm. For the models with $\rho_c = 2.9 \times 10^9$ g cm $^{-3}$ this radius corresponds to a density of $\rho_{\text{fuel}} = 2.2 \times 10^9$ g cm $^{-3}$. Models N300C and N1600C have a very compact and dense arrangement of the ignition kernels resulting in a setup of high spherical symmetry.

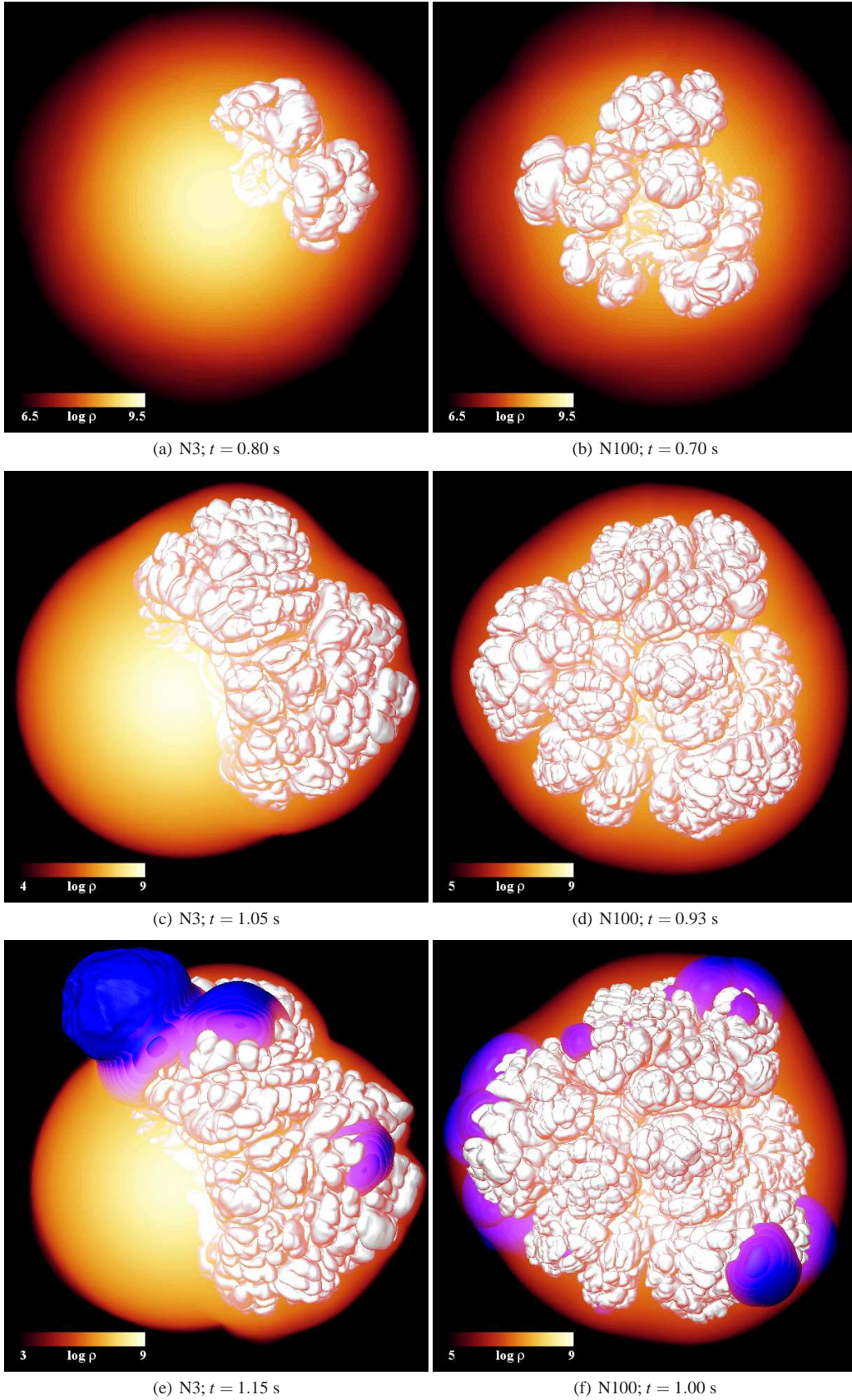


Figure 2. Snapshots of the hydrodynamic evolution of the N3 model (left column) and the N100 model (right column). The top row shows the rising plumes of the deflagration level set (white) during the Rayleigh-Taylor unstable stage of the deflagration phase embedded in a volume rendering of the density (in g cm^{-3}). The middle row shows the density and deflagration level set structure at the time the first DDT occurs. The bottom row shows the subsequent spreading of the detonation level set (blue) from the DDT initiation sites.

2012), it has been argued before that such a multi-spot ignition is a probable outcome of the convective carbon simmering phase leading up to the thermonuclear runaway (e.g. Garcia-Senz & Woosley 1995; Woosley et al. 2004; Iapichino et al. 2006). Such a configuration has numerical advantages because it gives rise to a broad spectrum of perturbations that seed the Rayleigh-Taylor instability, while smoother ignition geometries leave this to numerical discretization errors which depend on resolution (Röpke et al. 2007b). Regarding (ii), in cases with many ignition sparks we set off burning on different sides of the center. This corresponds to a nearly central ignition of the deflagration. In contrast, the recent simulations of Zingale et al. (2009) and Nonaka et al. (2012) suggest off-center ignitions due to a dominantly bipolar flow through the center. However, even slight rotation would disrupt the bipolar flow and consequently asymmetric ignition becomes less likely (Kuhlen et al. 2006). Even in the non-rotating case, for realistic Reynolds numbers ($\sim 10^{11}$ times larger than what is achieved in numerical simulations), the dipole pattern would likely give way to a highly turbulent and chaotic flow, which again would suggest a more symmetric ignition.

For this work we investigate a set of fourteen different explosion models, corresponding to different ignition setups that are summarized in Table 1. These setups are generated from a Monte-Carlo based algorithm. The main parameter of the ignition scenario is the number of spherical ignition kernels N_k that are aligned in the central area of the WD following a Gaussian distribution in radius. To avoid extreme outliers, we require that the ignition kernels have to be contained within a sphere of radius $R = 2.5\sigma$, where σ is the variance of the Gaussian distribution. We mention that for ignition models with low N_k the placement of the kernels cannot be considered as a real Gaussian distribution anymore. In particular model N1 with $N_k = 1$ constitutes a simple single off-center configuration where $R = \sigma$ holds. The ignition models N300C and N1600C (representing “compact” ignition configurations) are based on a configuration that has been used in Röpke et al. (2007a). By the generation of these models $R = 2.5\sigma$ holds, but after all ignition kernels are placed, the ones with a larger distance than σ are removed and replaced until for the whole configuration $R = \sigma$ holds (as in the case for $N_k = 1$). As a result we obtain a very dense and compact arrangement of the ignition kernels, where the whole configuration exhibits a highly spherical symmetry. We use a uniform radius for all ignition kernels set to $r_k = 10^6$ cm for all models except for the most centrally concentrated and compact ignition model N300C, where $r_k = 5 \times 10^5$ cm was used. The length d_k defines a minimum separation distance between the centers of the ignition kernels. Note that for large N_k , $r_k > d_k$, hence the ignition kernels may partially overlap, in particular in the vicinity of the center of the white dwarf. For a visualization of ignition setups see Fig. 1. We have chosen the ignition setups to obtain a suite of models covering a large range of strengths of the deflagration phase and associated pre-expansion of the WD prior to the onset of the detonation. This way, we obtain events that cover the same range of ^{56}Ni masses that is derived for normal SNe Ia in Stritzinger et al. (2006).

2.2 Computational method

All hydrodynamic explosion simulations presented here were performed with our thermonuclear supernova code LEAFS, a three-dimensional finite-volume discretization of the reactive Euler equations. The hydrodynamics solver is based on the PROMETHEUS implementation (Fryxell et al. 1989) of the “piecewise parabolic method” (PPM) by Colella & Woodward (1984).

Table 1. Parameters of the ignition setup of the deflagration.

Model	N_k	σ [10^7 cm]	r_k [10^6 cm]	d_k [10^6 cm]	ρ_c [10^9 g cm $^{-3}$]
N1	1	0.36	1.00	-	2.9
N3	3	0.50	1.00	3.00	2.9
N5	5	0.60	1.00	1.00	2.9
N10	10	0.60	1.00	1.00	2.9
N20	20	0.60	1.00	0.60	2.9
N40	40	0.60	1.00	1.00	2.9
N100L	100	0.60	1.00	0.30	1.0
N100	100	0.60	1.00	0.30	2.9
N100H	100	0.60	1.00	0.30	5.5
N150	150	0.60	1.00	0.35	2.9
N200	200	0.75	1.00	0.30	2.9
N300C	300	0.50	0.50	0.05	2.9
N1600	1600	1.00	1.00	0.05	2.9
N1600C	1600	1.80	1.00	0.05	2.9

Deflagration and detonation fronts are modeled as separate discontinuities between carbon-oxygen fuel and nuclear ash and their propagation is tracked with a level-set scheme (Reinecke et al. 1999; Osher & Sethian 1988; Smiljanovski et al. 1997). All material crossed by these fronts is converted to nuclear ash with a composition and energy release depending on fuel density. Although modeled with the same method, the propagation velocity, the ash composition and the nuclear energy release is different for deflagrations and detonations at a given fuel density. For detonations, the corresponding data is taken from the tables of Fink et al. (2010), and another table for deflagrations was determined in the same way as described there. In our hydrodynamic simulations, we model the composition of the material with only five species: carbon, oxygen, a representative proxy for an intermediate-mass isotope, and a mixture of nickel and alpha particles representing nuclear statistical equilibrium configurations. The latter are adjusted according to the prevailing thermodynamic conditions. We keep track of neutronization (and its effect on the equation of state) by following the evolution of Y_e as a separate and independent passive scalar.

The speed of the detonations is modeled as in Fink et al. (2010): at high densities ($\rho \gtrsim 10^7$ g cm $^{-3}$, pathological case), speeds are taken from Gamezo et al. (1999); at low densities, Chapman-Jouguet like speeds were calculated for the incomplete burning yields in our detonation tables. After a very short phase of laminar burning following ignition, the propagation of deflagrations is dominated by buoyancy and shear-induced instabilities and interactions with a complex turbulent flow field. The unresolved acceleration of the flame due to turbulence is accounted for by a sub-grid scale model (Schmidt et al. 2006a,b).

To follow the explosion ejecta to 100s, where homologous expansion becomes a good approximation, we employ a moving mesh technique (Röpke 2005; Röpke et al. 2006b) with an outer coarse inhomogeneous grid tracking the WD’s expansion and an inner finer homogeneous one encompassing the deflagration region. We include self-gravity with a monopole gravity solver. The total grid resolution is $512 \times 512 \times 512$ cells for all simulations presented here.

2.3 Criterion for deflagration to detonation transition (DDT)

Although details of the transition process from a subsonic deflagration to a supersonic detonation are not well under-

stood, it is generally believed that strong turbulent velocity fluctuations v' at the deflagration flame are required for a DDT to occur (Niemeyer & Woosley 1997; Lisewski et al. 2000; Woosley 2007; Woosley et al. 2009). Under this condition, mixed regions of hot burned and cold unburned material emerge that exceed a certain length scale of the order of $\ell_{\text{crit}} \approx 10^6$ cm (Dursi & Timmes 2006; Niemeyer & Woosley 1997; Khokhlov et al. 1997; Seitenzahl et al. 2009b). Based on the Zel'dovich gradient mechanism (Zel'dovich et al. 1970) a spontaneous ignition in such regions may lead to a sufficiently strong shock for the formation of a detonation front (Blinnikov & Khokhlov 1986; Khokhlov 1991a,b; Khokhlov et al. 1997; Seitenzahl et al. 2009a). Lisewski et al. (2000) pointed out that v' has to exceed 10^8 cm s $^{-1}$, but more recent studies of Woosley et al. (2009) suggested that smaller values of $v' \approx 5 \times 10^7$ cm s $^{-1}$ may be sufficient to trigger the DDT. In three-dimensional simulations of pure deflagrations Röpke (2007) found that the probability $P(v' \geq 10^8 \text{ cm s}^{-1})$ of finding v' of at least 10^8 cm s $^{-1}$ may be high enough for a DDT to occur.

The length scale ℓ_{crit} is not resolved in our large-scale simulations. Therefore a subgrid scale model is employed that evaluates the probability $P(v' \geq 10^8 \text{ cm s}^{-1})(t)$ at the time t at specific places at the deflagration flame that obey the following DDT constraints. To restrict our analysis to the immediate area of the flame, we define $X_{\text{fuel}} = 0.4\text{--}0.6$ as the allowed fuel fraction (the carbon/oxygen composition) in the grid cells, which ensures that the level set propagates on average through the center of these cells. We further define $\rho_{\text{fuel}} = (0.6\text{--}0.7) \times 10^7$ g cm $^{-3}$ as the allowed fuel densities in these cells, where this interval constitutes a subrange of the suggested fuel densities of Woosley (2007) where DDTs are expected to occur. The number $N_{\text{flame}}^*(t)$ and length $\Delta(t)$ of the grid cells that meet the above-mentioned constraints define a flame surface area $A_{\text{flame}}^*(t) = N_{\text{flame}}^*(t) \times (\Delta(t))^D$, where D is the fractal dimension. Following Kerstein (1988), Sreenivasan (1991) and Woosley (2007) we use $D = 2.36$. We define now $A_{\text{det}}(t) = P(v' \geq 10^8 \text{ cm s}^{-1})(t) \times A_{\text{flame}}^*(t)$ as the part of the flame that is capable of performing a DDT. If $A_{\text{det}}(t)$ exceeds a certain threshold A_{crit} (we use $A_{\text{crit}} = \ell_{\text{crit}}^D$, again with $D = 2.36$), it is checked whether this condition holds at least for half an eddy turnover time $\tau_{\text{eddy},1/2} = 0.5 \times \ell_{\text{crit}}/v' = 5 \times 10^{-3}$ s. This is to ensure that fuel and ash become sufficiently mixed on the scale ℓ_{crit} . If finally $A_{\text{det}}(t) \geq A_{\text{crit}}$ holds for $\tau_{\text{eddy},1/2}$, detonations are initialized in the grid cells that contain the highest velocity fluctuations, where the number of ignitions is given by the current ratio $A_{\text{det}}(t)$ to A_{crit} . This DDT criterion is consistent with findings of microscopical studies (Woosley 2007; Woosley et al. 2009) and is largely resolution-independent (for further details see Ciaraldi-Schoolmann & Röpke, in preparation).

2.4 Hydrodynamic evolution and explosion morphologies

First we point out that all fourteen simulations result in a completely gravitationally unbound remnant and are in this regard to be considered as “successful” explosions. The basic underlying evolution of all models is rather similar to other extant three-dimensional delayed detonation simulations.

The burning front propagates initially as a laminar conductive flame (Timmes & Woosley 1992). The nuclear burning releases energy by converting ^{12}C and ^{16}O to a mix of more tightly bound nuclei. This energy release is sufficient to at least partially lift the degeneracy of the burned material, which means that the ash is not only hotter but also less dense than the surrounding background

material. Buoyancy forces then lead to a rise of the deflagration ash material against gravity. Once the deflagration bubble exceeds a critical size it becomes subject to the Rayleigh-Taylor (RT) instability (e.g. Khokhlov 1995; Townsley et al. 2007), which wrinkles the flame front and causes a rapid acceleration of the growth of its surface area. As these RT-unstable plumes of hot deflagration ash continue to rise towards the stellar surface, the low Reynolds numbers coupled with the rather high relative speeds lead to Kelvin-Helmholtz induced shear on the sides of the rising plumes. This shear-induced turbulence in turn results in the high velocity fluctuations that lead to the fulfillment of our DDT criterion (see Sec. 2.3). The nascent detonation fronts propagate supersonically from their initiation sites and quickly burn any accessible (i.e. topologically connected, cf. Maier & Niemeyer 2006) fuel that remains above the respective density threshold to IMEs and IGEs. As an aside, we mention that the detonation level set may be advected into low density ($\rho < 5 \times 10^5$ g cm $^{-3}$) regions. However, this does not result in any burning there since we use the fuel density dependent energy release tables of Fink et al. (2010). Once the detonation has burned all remaining and accessible fuel, the supernova enters the stage of ballistic expansion. In Fig. 2 we show the morphology for two representative models (N3 and N100) at three different stages of the evolution.

Since we have essentially parametrized the strength of the deflagration phase by ignition kernel number (see Sec. 2.1 and Fig. 1), the models with the most ignition kernels burn the least amount of fuel in the detonation and vice versa (Röpke et al. 2007b; Mazzali et al. 2007; Kasen et al. 2009). Furthermore, it is evident that models with fewer ignition kernels are more asymmetric. A prime example for this is N3, see left column of Fig. 2. The small number of ignition kernels necessarily leads to a highly asymmetric seed configuration of the RT-unstable deflagration plumes, which results in a highly asymmetric distribution of the deflagration ashes in the star. For our N3 case, only one hemisphere is burned by the deflagration. The fact that the detonation can only be triggered at the interface of the deflagration flame front and the fuel reinforces this asymmetry. The resulting distribution of the nucleosynthesis products fully reflects the asymmetric evolution of the deflagration and detonation (see Fig. 3). In contrast, consider the N100 model (right column in Fig. 2). The rather symmetric ignition configuration results in deflagration plumes rising in all directions. As a consequence, DDTs also occur on all sides of the star and the explosion asymmetries are very modest, which again reflects in a more symmetric distribution of burning products (see Fig. 4).

3 NUCLEOSYNTHESIS

For each of the fourteen models, we have determined the isotopic composition of the ejecta using our tracer particle method (Travaglio et al. 2004; Röpke et al. 2006a; Seitenzahl et al. 2010). In each initial model we have distributed one million tracer particles of equal mass in a way that the underlying density profile of the WD is reproduced by the tracer particles. Extrapolating the tracer resolution and yield convergence study (done in 2D) of Seitenzahl et al. (2010) to 3D, this number of tracer particles (100 per axis) is sufficient to reliably predict the yields for the most abundant nuclides. For all models, the initial chemical composition for the post-processing is taken to be 47.5 per cent ^{12}C , 50 per cent ^{16}O , and 2.5 per cent ^{22}Ne by mass. The ^{22}Ne fraction roughly corresponds to solar metallicity of the zero-age main-sequence progenitor under the often made approxima-

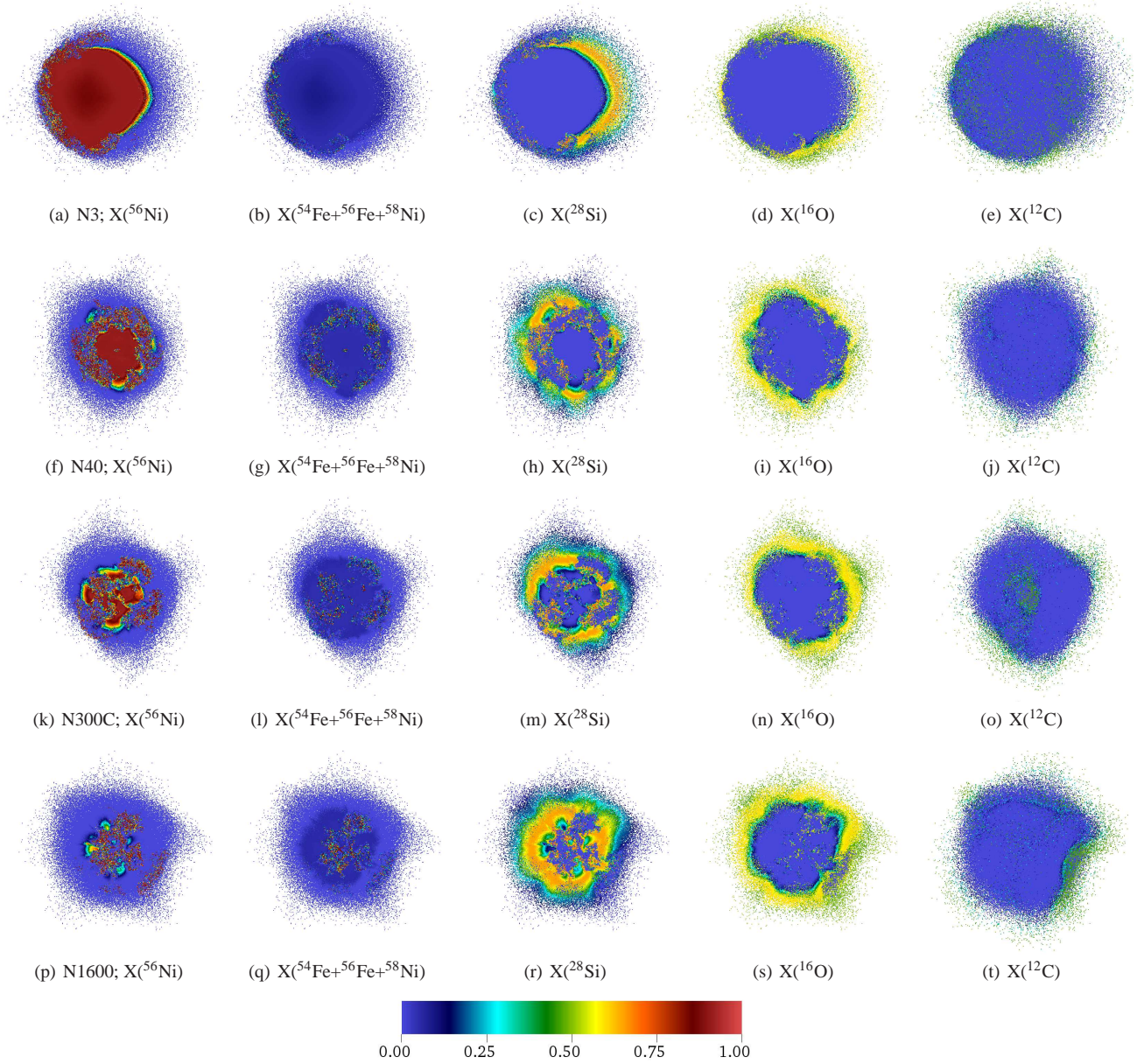


Figure 3. Tracer particle positions for the N3, N40, N300C, and N1600 models (from top to bottom). The tracer particles are colored by the mass fractions of ^{56}Ni (first column), $^{54}\text{Fe}+^{56}\text{Fe}+^{58}\text{Ni}$ (representing stable iron group nuclei, second column), ^{28}Si (third column), ^{16}O (fourth column) and ^{12}C (fifth column) at $t = 100$ s. For ^{56}Ni , ^{28}Si , ^{16}O and the stable iron group nuclei, the tracer particle cloud is cut in the plane of the page and only the bottom hemisphere is shown. Plotting the data this way allows the viewer to also see the abundance distributions in the deep core while still retaining the three dimensional nature of the tracer particle locations. Only for ^{12}C the full spherical cloud is shown since ^{12}C largely resides near the surface.

tion that ^{14}N is processed to ^{22}Ne during core helium burning via $^{14}\text{N}(\alpha, \gamma)^{18}\text{F}(\beta^+)^{18}\text{O}(\alpha, \gamma)^{22}\text{Ne}$. The ^{22}Ne content introduces an excess of neutrons and results in an electron fraction of $Y_e = 0.49886$. This composition is assumed to be homogeneous throughout the star. The yield distributions can be used as an input to radiative transfer calculations (e.g. Kasen et al. 2006; Sim 2007; Sim et al. 2010; Kromer et al. 2010; Pakmor et al. 2010; Röpke et al. 2012) to derive model light curves and spectra. Furthermore, the yields can be used as an input for galactic chemical evolution calculations or to make predictions of the shapes of the late-time light curves (e.g. Seitenzahl et al. 2009c; Seitenzahl 2011; Röpke et al. 2012).

3.1 Total integrated nucleosynthetic yields

The yields of stable nuclides are presented in Table 2. For this table we have completely decayed all radioactive nuclides with half-lives less than 2 Gyr (such as ^{40}K or ^{53}Mn) to stability; nuclides with half-lives longer than 2 Gyr (i.e. ^{50}V) are tabulated with their production yields at $t = 100$ s. The yields at $t = 100$ s of some abundant and long-lived radioactive nuclides are tabulated in Table 3. For convenience, we also show the yields of ^{56}Ni , IGEs, IMEs, ^{16}O , and ^{12}C in Fig. 5

We note a few obvious trends in the total integrated yields. As expected, there is a clear trend that the total mass of ^{56}Ni produced

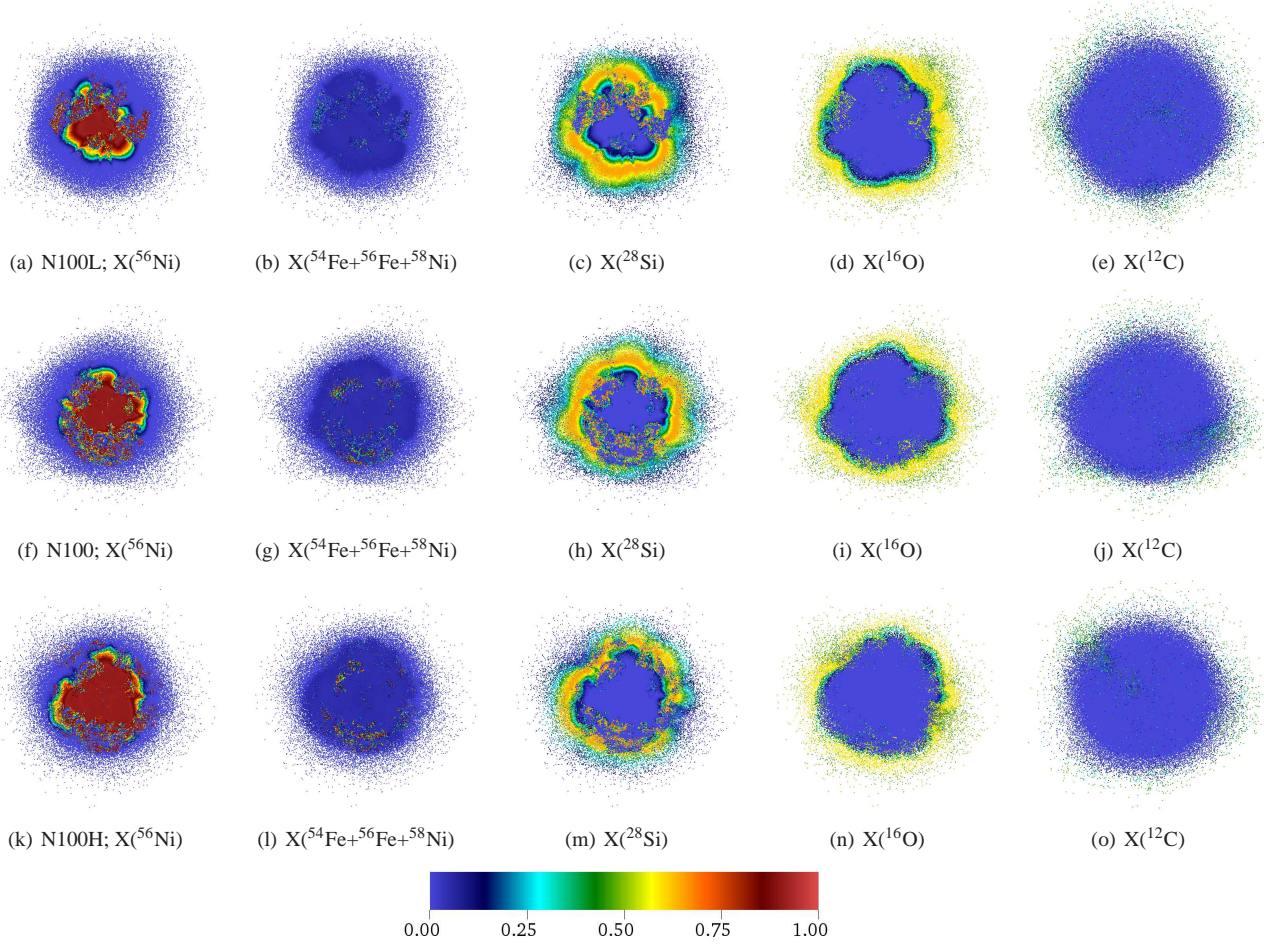


Figure 4. Tracer particle positions for the central density sequence of N100 models (from the low central density N100L model in the top row to the high central density model N100H in the bottom row). Just as in Fig. 3 the tracer particles are colored by the mass fractions of ^{56}Ni (first column), $^{54}\text{Fe}+^{56}\text{Fe}+^{58}\text{Ni}$ (representing stable iron group nuclei, second column), ^{28}Si (third column), ^{16}O (forth column) and ^{12}C (fifth column) at $t = 100$ s. Again, for ^{12}C we show the whole cloud of tracer particles, whereas only one hemisphere is shown for all other species.

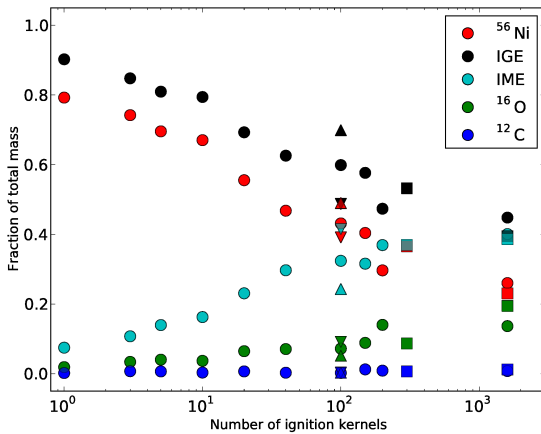


Figure 5. Fraction of the total mass at $t = 100$ s in ^{56}Ni , IGEs (including ^{56}Ni), IMEs, ^{16}O , and ^{12}C as a function of ignition kernel number. We use upward-pointing triangles for N100H, downward-pointing triangles for N100L, squares for N300C and N1600C, and circles for all other models.

decreases with increasing ignition kernel number – from $1.11 M_{\odot}$ for N1 down to $0.32 M_{\odot}$ for N1600C. This covers the range of expected ^{56}Ni masses of normal SNe Ia (Stritzinger et al. 2006). Similarly, the total mass produced as intermediate mass elements (see e.g. ^{28}Si or ^{32}Si) shows a clear trend of increasing yields with increasing ignition kernel number.

This can be understood in the following way. For small numbers of ignition kernels, the deflagration is relatively weak and burns only a small fraction of the total mass of the star. The associated energy release results in only moderately strong expansion. Consequently, at the first occurrence of a DDT, the central density of the WD is still quite high and most of the remaining fuel will be burned to IGE (most of which is ^{56}Ni) by the detonation. In contrast, the larger the number of ignition sparks, the stronger is the expansion during the deflagration phase. The low central density at the onset of the first DDT now results in much of the remaining fuel to be located below a density of $1 \times 10^7 \text{ g cm}^{-3}$, approximately the cutoff where a detonation in equal mass carbon-oxygen material ceases to burn completely to NSE and instead produces IMEs as a result of incomplete burning.

^{58}Ni , which is by far the most abundant stable nickel isotope in all models, shows remarkably little variation. The models produce ^{58}Ni masses from 6.2 to $7.5 \times 10^{-2} M_{\odot}$. The only exception is

the low central density model N100L, which undergoes less in situ neutronization and only synthesizes $3.8 \times 10^{-2} M_{\odot}$ of ^{58}Ni .

While estimated ^{56}Ni masses of SNe Ia cover quite a range, most observed events cluster around $0.6 M_{\odot}$ (e.g. Stritzinger et al. 2006). For this reason, we have chosen the three N100 models for a comparison of their isotopic iron peak production factors with the solar values, $(X_{AZ}/X_{56\text{Fe}})/(X_{AZ}/X_{56\text{Fe}})_{\odot}$ (see Fig. 6). For the solar composition we use Lodders (2003). Our model production factors exhibit qualitatively the right behavior that is required for SN Ia yields: production factors of self-conjugate and slightly neutron rich isotopes ^{50}Cr , ^{51}Cr , ^{52}Cr , ^{55}Mn , ^{54}Fe , and ^{58}Ni only weakly depend on the particular choice of central density of the WD at the time of ignition. These isotopes are expected to be largely synthesized in nuclear statistical equilibrium in SNe Ia, which requires production factors $\gtrsim 1$ as observed here. Large overproduction factors ($[^{A}Z/^{56}\text{Fe}] \gtrsim 2$), are marginally in conflict with the requirement that SNe Ia produced roughly half of the ^{56}Fe present in the Sun today (Clayton 2003). We note, however, that models with different central density at ignition yield lower overproduction factors (Fig. 6) and that lower progenitor metallicities also results in less neutron rich iron group isotopes (see Section 3.2).

The only isotope with an overproduction factor > 3 is ^{54}Cr for the high central density model N100H. We interpret the large overproduction factor we obtain there as an indication that delayed detonation SNe Ia that ignite at central densities $\gtrsim 5.5 \times 10^9 \text{ g cm}^{-3}$ are rare and constitute at most a small fraction of all SN Ia events. The most neutron-rich stable Fe-peak isotopes ^{54}Cr , ^{58}Fe , and ^{64}Ni are shielded by ^{54}Fe , ^{58}Ni , and ^{64}Zn from the $Z = N$ line and thus require the most neutronization for direct production. Consequently, these isotopes are the most sensitive to the central density, with the highest production factors occurring for the N100H model. The very pronounced underproduction of ^{58}Fe and ^{64}Ni in all the models is not a problem, since the S-process is the dominant source of nucleosynthesis for these isotopes. The solar abundances of the remaining isotopes ^{59}Co , ^{60}Ni , ^{61}Ni , and ^{62}Ni contain significant contributions from explosive Si-burning (core collapse SNe), alpha-rich freeze-out (including SNe Ia), and the S-process. Our production factors for SNe Ia on the order of a few to several tens of percent are therefore also very reasonable.

For a detailed discussion of the nucleosynthesis origin in the Sun of the isotopes discussed here see the book by Clayton (2003), which we have used as a reference for our comparison.

The subset of our three N100 models contains another interesting trend. We find that the ^{56}Ni mass in the N100 model sequence increases with central density, i.e. the high central density model N100H produces the most and the low central density model N100L produces the least amount of ^{56}Ni . This is exactly opposite to the behavior found by Krueger et al. (2010) when they analyzed their statistical sample of 150 two-dimensional delayed-detonation explosion simulations. They considered a range of central ignition densities (1 to $5 \times 10^9 \text{ g cm}^{-3}$), a fixed deflagration to detonation transition density of $10^{7.1} \text{ g cm}^{-3}$, but did not perform post-processing with a detailed nuclear reaction network.

In our models, the fraction of NSE material (for a recent discussion of NSE in SN Ia see Seitenzahl et al. 2009d) that is produced as ^{56}Ni is highest for the low central density model and lowest for the high central density model, which is what is expected. The total amount of iron group material synthesized is, however, strongly increasing with central density. We have seen the same trend already in Seitenzahl et al. (2011), where we had estimated a roughly constant ^{56}Ni yield as a function of central density. The ^{56}Ni mass in that work was derived from the total mass

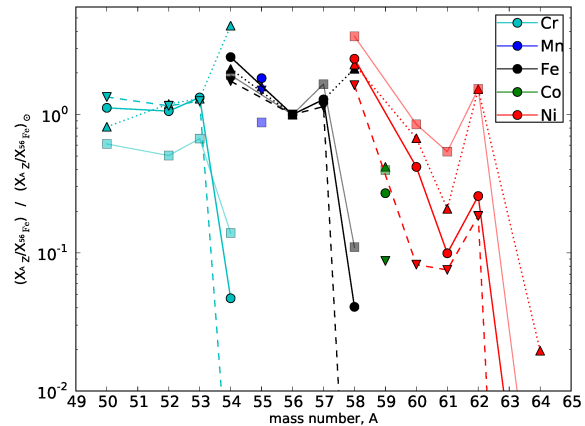


Figure 6. Production factors $(X_{AZ}/X_{56\text{Fe}})/(X_{AZ}/X_{56\text{Fe}})_{\odot}$ of stable iron peak isotopes relative to ^{56}Fe normalized to the corresponding solar values (Lodders 2003) for models N100L (downward-pointing triangles/dashed lines), N100 (circles/solid lines), and N100H (upward-pointing triangles/dotted lines) and W7 (transparent squares/thin solid lines; Maeda et al. 2010b). The lower the central density, the smaller the overproduction of ^{54}Fe and ^{58}Ni .

in IGE and the electron fraction Y_e , essentially using the formula in Timmes et al. (2003). Here we determine the nucleosynthesis in detail with one million tracer particles and we find that the ^{56}Ni mass increases with increasing central density. We caution, however, that our sample consisting of three models in a single ignition configuration is not statistically significant.

3.2 Dependence of yields on progenitor metallicity

To assess the impact of varying the progenitor metallicity, we have also post-processed the N100 model with one-half, one tenth, and one hundredth of the canonical ^{22}Ne mass fraction of 0.025. The ^{12}C mass fractions were thus 0.4875, 0.4975 and 0.49975 and $X(^{16}\text{O})$ was kept constant at 0.5. The models with reduced ^{22}Ne are called N100_Z0.5, N100_Z0.1, and N100_Z0.01 respectively and their yields are also presented in Tables 2 and 3.

As expected (Timmes et al. 2003; Travaglio et al. 2005), the ^{56}Ni yields increase with decreasing initial ^{22}Ne due to the decreasing electron fraction Y_e , largely at the cost of stable iron group isotopes such as ^{58}Ni or ^{54}Fe . As a consequence, the overproduction factors of these isotopes are successively reduced to $\lesssim 2$ even for the canonical central density case (Fig. 7). Since the ^{56}Fe in the Sun is largely due to supernovae that had progenitors with sub-solar metallicity, we argue that the isotopic Fe-group yields of our delayed-detonations are not inconsistent with solar isotopic ratios.

3.3 Spatial and velocity distribution of nucleosynthetic yields

Total integrated yields constitute very important predictions and diagnostics for an explosion model. How the yields are distributed in mass and velocity space is, however, at least equally important, especially when it comes to direct observables of the supernova such as spectra or light curves.

It is not possible to show the spatial yield distributions of all nuclei for all models. Therefore, we restrict ourselves to show only ^{56}Ni (as the main source of radioactive heating), $^{54}\text{Fe}+^{56}\text{Fe}+^{58}\text{Ni}$

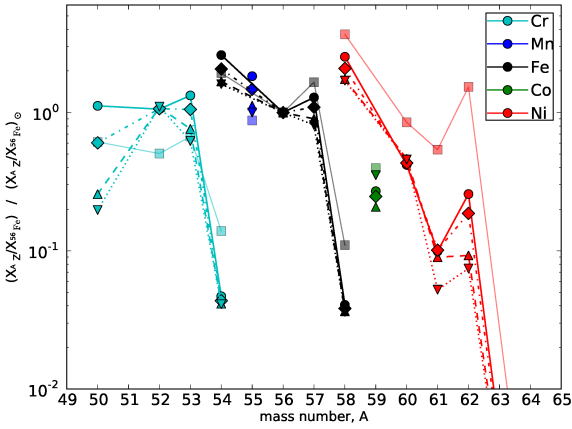


Figure 7. Production factors $(X_{AZ}/X_{56Fe})/(X_{AZ}/X_{56Fe})_{\odot}$ of stable iron peak isotopes relative to ^{56}Fe normalized to the corresponding solar values (Lodders 2003) for models N100 (circles/solid lines), N100_Z0.5 (diamonds/dot-dashed lines), N100_Z0.1 (upward-pointing triangles/dashed lines), N100_Z0.01 (downward-pointing triangles/dotted lines) and W7 (transparent squares/thin solid lines; Maeda et al. 2010b). The smaller the initial ^{22}Ne mass fraction, the smaller the overproduction of ^{54}Fe , ^{55}Mn , and ^{58}Ni .

(as most abundant stable IGEs and important sources of opacity), ^{28}Si (as the generally most abundant intermediate mass isotope) and the fuel isotopes ^{16}O and ^{12}C , for a representative sample of the four models N3, N40, N300C, and N1600 (see Fig. 3). Globally, the abundances are stratified as is expected for delayed-detonations: Near the surface some unburned carbon sits on top of an oxygen-rich layer that is composed of unburned oxygen fuel and products of low-density carbon burning. Further inwards IMEs such as ^{28}Si and ^{32}S are the most abundant species, although a strict onion-shell structure as is seen in one-dimensional models is not present. Instead, Rayleigh-Taylor plumes of material rich in stable IGEs have penetrated into this layer. Consequently, stable IGEs are not found at the lowest velocities as predicted by one-dimensional models (e.g. Nomoto et al. 1984; Khokhlov 1991c; Höflich et al. 2004), but rather at intermediate velocities ($\sim 3,000 - 10,000 \text{ km s}^{-1}$). This agrees well with the results of Maeda et al. (2010b), who find typical velocities of $5,000 - 10,000 \text{ km s}^{-1}$ for the deflagration ash in their two-dimensional O-DDT model. This signature of the burning in the deflagration is characteristic to multi-dimensional simulations that are not ignited at the very center. Unlike in the one-dimensional case, the hot, less dense, buoyant ash can float towards the surface. We note that Stehle et al. (2005) find substantial amounts of stable iron out to velocities of about $9,000 \text{ km s}^{-1}$ analyzing spectra of SN 2002bo. In contrast to our model of comparable brightness (N100), in their abundance tomography, which is based on one-dimensional explosion models, the abundance of stable iron increases steadily towards lower velocities and dominates in the very center.

In between the IGE-rich plumes, small pockets filled with oxygen-rich material remain – these were downdrafts in the deflagration that were burned only in the latest phases of the detonation at low densities. The central regions, on the other hand, which were burned by the detonation at high densities to NSE, form a homogeneous ^{56}Ni clump. In the fainter models, this clump fragments progressively. This is a natural consequence of the fact that in these models the majority of IGE material is produced by the deflagra-

tion and not by the detonation. In these models, the strong initial expansion due to the deflagration results in such low densities in the core that the ensuing detonation fails to process this material to NSE (see Fig. 3(p)). We also show the same set of mass fractions for the three N100 models (see Fig. 4). The global picture of chemical stratification discussed above is rather insensitive to central ignition density.

To better visualize the underlying main trends of the whole model suite, and to facilitate a comparison of the three-dimensional models, we reduce the information and show one-dimensional abundance profiles in velocity space (see Fig. 8). We emphasize that this averaging or binning of the three dimensional data erases all information about the inhomogeneities and (sometimes pronounced) asymmetries brought about by e.g. the rising plumes of deflagration ash or downdrafts of nuclear fuel. This is also true for models with a strong (turbulent) deflagration phase, which are rather symmetric under rotations on large scales, but exhibit strong inhomogeneities in the burning products on small scales (see the different morphology plots in Sec. 2.4). For example, the presence of e.g. ^{16}O and ^{56}Ni in these one-dimensional profiles at the same velocity does not necessarily imply a co-spatial existence of these nuclear species.

Kozma et al. (2005) showed that ejecta with oxygen at low velocities (as we find it for our models with large N_k) may lead to strong $[\text{O I}] \lambda\lambda 6300, 6364$ emission at late times, which is not observed in SNe Ia. The mere presence of oxygen at low velocities, however, is not the only relevant condition for $[\text{O I}]$ emission. Whether $[\text{O I}]$ features will arise, depends strongly on the ionisation state and a possible microscopic mixing of different species. Compared to the deflagration model of Kozma et al. (2005), our delayed detonation models have lower density ejecta, which could lead to a higher ionization. The question of microscopic mixing cannot be answered from present-day numerical models since it takes place on scales which are not resolved. However, if such a mixing is present, stronger transitions than $[\text{O I}]$ will dominate the cooling.

As a general trend, ^{56}Ni is hardly present at velocities above $\sim 12,000 \text{ km s}^{-1}$.¹ The exceptions are the models N3 and N5, where parts of the asymmetrically rising deflagration plumes have already risen to the stellar surface when the first DDT occurs (see Fig. 2c). In these models, the deflagration ash is therefore not completely enclosed by burning products of the detonation and there is some ^{56}Ni present at very high velocity. ^{57}Ni and ^{58}Ni are produced co-spatially with ^{56}Ni and more or less follow its distribution, albeit with a lower abundance.

The distribution of IMEs in velocity space shows a clear trend with ignition kernel number. The brightest models (small number of ignition kernels) contain IMEs from the highest expansion velocities down to $\sim 6,000 - 7,000 \text{ km s}^{-1}$. For the fainter models (larger number of ignition kernels) the inner boundary of the IMEs continues to move inward and the IMEs at the highest velocities are more and more replaced by unburned fuel (see also Mazzali et al. 2007).

Notably, carbon and oxygen are extending down to low velocities. There is always some carbon present down to or even below velocities of $12,000 \text{ km s}^{-1}$. Note that this is much lower than what has been found for W7 (Nomoto et al. 1984; Iwamoto et al. 1999; Maeda et al. 2010b). Oxygen reaches down even farther, always present below $\sim 8,000 \text{ km s}^{-1}$ and sometimes even reaching

¹ One should be aware of the fact that already traces of IGEs on the equivalent level of solar abundance may affect the observables significantly.

to the very center. The presence of unburned fuel in our models is a distinct multi-dimensional effect. For fainter models, the products of low-density detonation burning extend down to lower velocities. In extreme cases, pockets of unburned fuel remain near the center that are not reached by the detonation at all.

The other abundant iron group isotopes ^{55}Co , ^{54}Fe , and ^{56}Fe are mainly produced in the deflagration phase. As a result, they are concentrated in an off center shell surrounding the central ^{56}Ni bubble (see Figs. 3–8). Only models with a weak deflagration phase (in particular N1, N3, N5) exhibit high enough central densities during the detonation phase that some neutronization and normal freeze-out from NSE also synthesizes significant amounts of these isotopes in a second, centrally concentrated production site (see Fig. 8).

The idea suggests itself to compare the yield morphologies of our three-dimensional simulations to existing two-dimensional results from the literature. Such a comparison, however, is difficult to make quantitatively. For example, the results of Kasen et al. (2006) were not based on detailed yield information obtained by post-processing each model but mapped representative yields into the individual realizations. A qualitative discussion, however, is possible: Comparing Fig. 3 to their figure 1, we can, however, identify a key commonality. In both sets, the stable IGEs in bright models are most abundant at intermediate velocities, surrounding a core rich in ^{56}Ni . Conversely, the fainter models have the stable IGE much closer to the center. To the best of our knowledge, the only published results of multi-dimensional delayed-detonations with detailed nucleosynthetic yields are the two models of Maeda et al. (2010b). A meaningful comparison to their C-DDT model, which is based on a rather symmetrically and centrally ignited deflagration, is not possible. In their C-DDT model, the DDT occurs at such a late time and low density that no more ^{56}Ni is produced by the detonation wave, resulting in a very low mass of final ^{56}Ni of $\sim 0.25 M_{\odot}$. This is both outside the range of ^{56}Ni masses covered by our models as well as observed “normal” SNe Ia. On the other hand, their O-DDT model, which is based on an asymmetric ignition of the deflagration, produces $\sim 0.54 M_{\odot}$ of ^{56}Ni , which is rather similar to our N150 or N100 models. In spite of the different symmetries in the ignition configuration, the angle averaged distribution of nuclides in velocity space (compare figure 11(c) of Maeda et al. (2010b) and Fig. 3) are quite similar. In both O-DDT and our models, the lowest velocities are dominated by ^{56}Ni and ^{58}Ni , IMEs are present down to velocities of a few thousand km s^{-1} , ^{16}O down to just below $5,000 \text{ km s}^{-1}$, and unburned ^{12}C down to around $\sim 10,000 \text{ km s}^{-1}$. Stable IGE are only found at intermediate velocities between $\sim 5,000 - 11,000 \text{ km s}^{-1}$, and ^{56}Ni cuts off sharply around $11,000 \text{ km s}^{-1}$.

In 2D axisymmetric simulations, the rising deflagration “bubbles” are in fact “tori”. This leads to differences in the morphology, even if angle averages look alike. 3D models allow for variation on smaller angular scales. A rising torus is a more symmetric and also more extended object than a rising bubble. Since it contains much more volume than a single bubble, a 2D deflagration starting from the same ignition site releases more energy and is more symmetric than the corresponding case in 3D. This may explain why the 2D O-DDT model, which was ignited in a rather asymmetric configuration in only 29 spots, ends up looking rather symmetric and not nearly as bright as e.g. our N20 or N40 model.

4 SUMMARY AND CONCLUSIONS

We have performed fourteen three-dimensional hydrodynamical simulations for delayed detonation SNe Ia for a range of ignition conditions. For each simulation we have determined the complete nucleosynthetic yields by post-processing one million tracer particles with a nuclear reaction network. This set of models constitutes the first suite of three-dimensional explosion models that covers the range of expected ^{56}Ni masses of spectroscopically normal SNe Ia. From our study we conclude that, fixing all other parameters of the exploding WD but the ignition configuration, a delayed-detonation of “normal” SN Ia brightness likely requires rather symmetrical, central ignition to occur in nature. Only such a setup sufficiently pre-expands the WD in the deflagration phase to reduce the ^{56}Ni production in the subsequent detonation. Otherwise only the brightest SNe Ia could be explained with delayed detonations of Chandrasekhar-mass WDs as realized in our models by few (and thus asymmetrically distributed) ignition sparks. Whether or not the demand for symmetric ignition is in conflict with Maeda et al. (2010a), who require a typical off-set of $\sim 3,500 \text{ km s}^{-1}$ in the deflagration ashes, is not clear. In spite of rather symmetric ignition in our “normal” models, the fact that one or a few RT-modes grow faster than the others still results in a distribution of stable Fe-peak isotopes that is not uniform (see second column of Fig. 4).

Our suite of models is the first published set of three-dimensional delayed detonation simulations with detailed isotopic nucleosynthetic yields. As such, the yields presented here lend themselves to be used as an input for Galactic chemical evolution calculations. They also set the stage for predicting observables by radiative transfer calculations. Overall, we expect the brightness range of normal SNe Ia to be covered by our set of models. It remains to be seen whether the predicted spectra match the observations and whether the set of models follows the width-luminosity relation (Phillips 1993; Phillips et al. 1999) and other observational trends, as a set of two-dimensional delayed-detonation models did (Kasen et al. 2009; Blondin et al. 2011). The Fe-group isotopes in our models of normal SN Ia brightness (^{56}Ni masses around $0.6 M_{\odot}$) are synthesized in the required proportions (see Figs. 6 and 7), which tells us that delayed-detonations cannot be ruled out as the dominant SN Ia explosion channel based on solar isotopic Fe-group ratios. The presence of IGEs (in particular stable isotopes) at high velocities and oxygen and carbon in the inner ejecta in our models is expected to leave testable imprints on the observables. Moreover, our set of three-dimensional full-star models captures asymmetries that potentially could be constrained by spectropolarimetry measurements (see e.g. the review by Wang & Wheeler 2008).

ACKNOWLEDGEMENTS

The simulations presented here were carried out in part on the JUGENE supercomputer at the Forschungszentrum Jülich within the Partnership for Advanced Computing in Europe (PRA042), the grant HMU13 and in part at the Computer Center of the Max Planck Society, Garching, Germany. This work was also supported by the Deutsche Forschungsgemeinschaft via the Transregional Collaborative Research Center TRR 33 “The Dark Universe”, the Emmy Noether Program (RO 3676/1-1), the ARCHES prize of the German Ministry of Education and Research (BMBF), the graduate school “Theoretical Astrophysics and Particle Physics” at the University of Würzburg (GRK 1147) and the Excellence Cluster

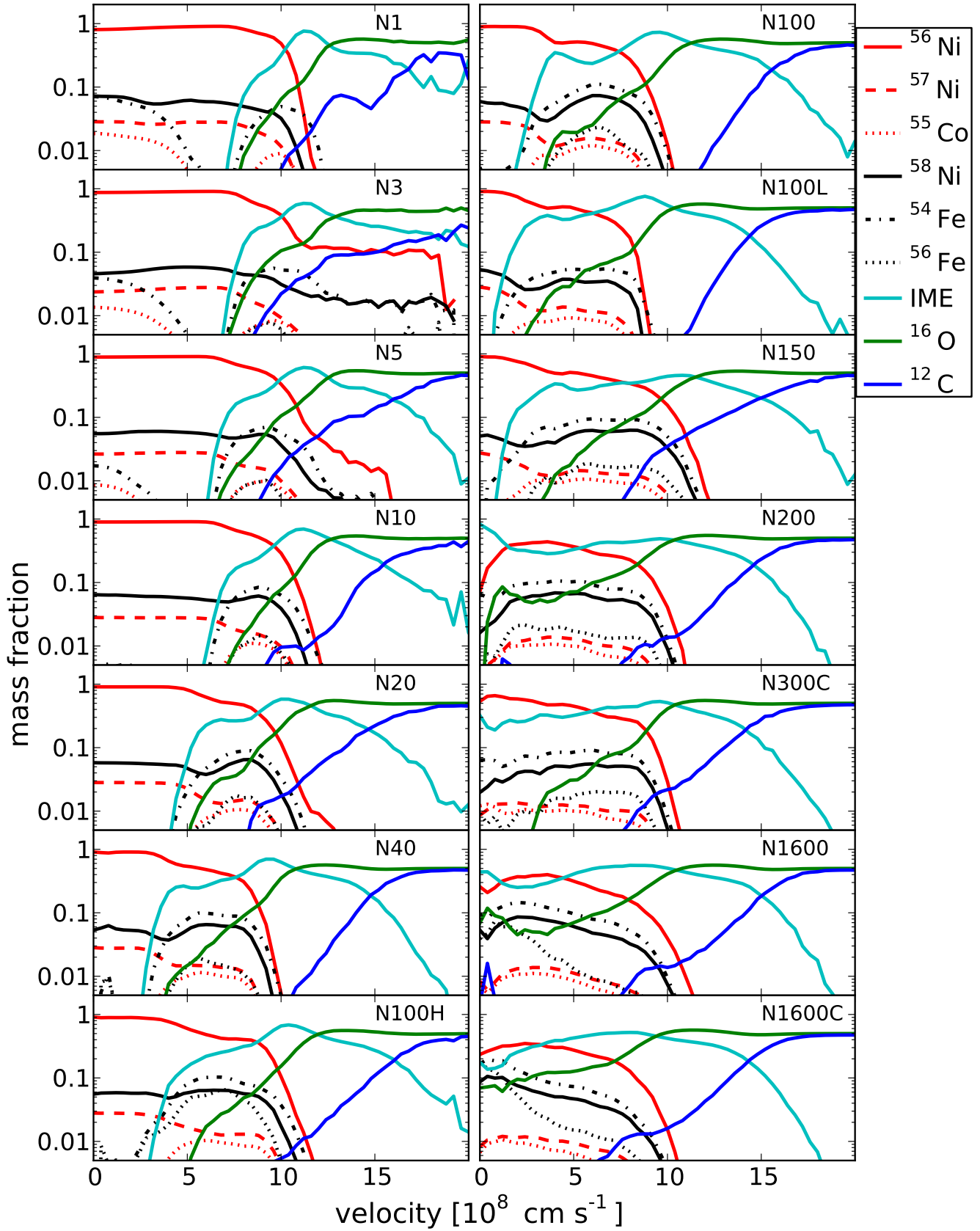


Figure 8. Shown are average mass fractions of some select isotopes and IME at time $t = 100 \text{ s}$ in velocity space.

Table 2. Asymptotic nucleosynthetic yields (in solar masses) of stable nuclides.

	N1	N3	N5	N10	N20	N40	N100H	N100	N100L	N150	N200	N300C	N1600	N1600C	N100_Z0.5	N100_Z0.1	N100_Z0.01
¹² C	2.61E-03	9.90E-03	9.05E-03	4.43E-03	9.20E-03	3.90E-03	3.87E-03	3.04E-03	3.85E-03	1.72E-02	1.21E-02	8.86E-03	1.06E-02	1.68E-02	3.10e-03	3.15e-03	3.16e-03
¹³ C	1.84E-08	6.15E-08	5.05E-08	2.57E-08	4.52E-08	2.18E-08	2.28E-08	1.74E-08	2.17E-08	1.00E-07	6.57E-08	4.95E-08	5.57E-08	8.44E-08	8.47e-09	1.91e-09	2.72e-10
¹⁴ N	2.92E-06	9.93E-06	8.46E-06	3.85E-06	8.34E-06	4.30E-06	4.25E-06	3.21E-06	3.98E-06	1.84E-05	1.33E-05	9.16E-06	1.04E-05	1.88E-05	1.80e-06	4.71e-07	7.22e-08
¹⁵ N	3.36E-09	1.22E-08	1.03E-08	4.47E-09	1.03E-08	5.16E-09	5.24E-09	3.67E-09	4.66E-09	2.29E-08	1.71E-08	1.14E-08	1.29E-08	2.41E-08	2.07e-09	2.98e-09	8.73e-08
¹⁶ O	2.63E-02	4.74E-02	5.63E-02	5.16E-02	9.04E-02	9.89E-02	7.30E-02	1.01E-01	1.24E-01	1.24E-01	1.96E-01	1.21E-01	1.91E-01	2.72E-01	9.87e-02	9.64e-02	9.47e-02
¹⁷ O	3.96E-07	1.37E-06	1.16E-06	5.34E-07	1.12E-06	5.54E-07	5.61E-07	4.13E-07	5.14E-07	2.48E-06	1.74E-06	1.22E-06	1.36E-06	2.42E-06	2.84e-07	9.32e-08	5.43e-09
¹⁸ O	3.32E-09	1.33E-08	1.11E-08	4.54E-09	1.12E-08	5.29E-09	5.59E-09	3.53E-09	4.61E-09	2.52E-08	1.98E-08	1.25E-08	1.44E-08	2.73E-08	2.23e-09	1.21e-09	9.93e-10
¹⁹ F	3.73E-11	1.35E-10	1.17E-10	5.05E-11	1.22E-10	6.22E-11	6.32E-11	4.39E-11	5.68E-11	2.64E-10	2.13E-10	1.36E-10	1.58E-10	2.97E-10	2.20e-11	1.48e-11	4.79e-11
²⁰ Ne	1.47E-03	3.37E-03	3.75E-03	2.40E-03	5.41E-03	4.15E-03	3.66E-03	3.53E-03	4.33E-03	8.72E-03	1.15E-02	6.76E-03	9.40E-03	1.73E-02	3.60e-03	3.69e-03	3.74e-03
²¹ Ne	3.08E-07	9.79E-07	8.81E-07	4.16E-07	9.63E-07	5.43E-07	5.20E-07	4.11E-07	5.17E-07	1.98E-06	1.68E-06	1.08E-06	1.29E-06	2.39E-06	1.97e-07	4.47e-08	6.93e-09
²² Ne	6.40E-05	3.26E-04	2.87E-04	1.31E-04	2.58E-04	5.77E-05	7.62E-05	4.07E-05	5.51E-05	4.83E-04	2.34E-04	2.11E-04	2.32E-04	2.97E-04	1.65e-05	2.30e-06	1.71e-07
²³ Na	2.20E-05	6.41E-05	6.09E-05	3.22E-05	7.30E-05	4.66E-05	4.25E-05	3.74E-05	4.68E-05	1.38E-04	1.38E-04	8.53E-05	1.09E-04	2.02E-04	2.63e-05	1.96e-05	1.72e-05
²⁴ Mg	3.93E-03	7.13E-03	8.53E-03	7.77E-03	1.46E-02	1.54E-02	1.15E-02	1.52E-02	1.83E-02	1.93E-02	3.32E-02	1.97E-02	3.08E-02	4.64E-02	2.02e-02	2.69e-02	2.90e-02
²⁵ Mg	3.35E-05	9.26E-05	8.92E-05	5.07E-05	1.11E-04	7.70E-05	6.86E-05	6.49E-05	8.02E-05	2.02E-04	2.14E-04	1.33E-04	1.75E-04	3.12E-04	3.09e-05	1.06e-05	8.99e-07
²⁶ Mg	5.15E-05	1.36E-04	1.34E-04	7.55E-05	1.71E-04	1.17E-04	1.04E-04	9.66E-05	1.19E-04	3.07E-04	3.27E-04	2.01E-04	2.63E-04	4.82E-04	4.44e-05	7.36e-06	1.04e-06
²⁷ Al	1.98E-04	3.95E-04	4.56E-04	3.71E-04	7.32E-04	7.05E-04	5.47E-04	6.74E-04	8.32E-04	1.04E-03	1.64E-03	9.68E-04	1.48E-03	2.37E-03	5.88e-04	2.68e-04	8.71e-05
²⁸ Si	6.32E-02	8.99E-02	1.19E-01	1.38E-01	1.98E-01	2.59E-01	2.12E-01	2.84E-01	3.55E-01	2.71E-01	3.28E-01	3.19E-01	3.61E-01	3.44E-01	2.90e-01	2.94e-01	2.89e-01
²⁹ Si	2.69E-04	4.64E-04	5.68E-04	5.17E-04	9.49E-04	1.03E-03	7.73E-04	1.03E-03	1.25E-03	1.30E-03	2.08E-03	1.29E-03	1.97E-03	2.86E-03	7.28e-04	4.30e-04	1.35e-04
³⁰ Si	5.96E-04	1.00E-03	1.23E-03	1.18E-03	2.12E-03	2.35E-03	1.72E-03	2.36E-03	2.86E-03	2.77E-03	4.76E-03	2.87E-03	4.53E-03	6.55E-03	1.19e-03	1.44e-04	1.84e-05
³¹ P	1.40E-04	2.28E-04	2.87E-04	2.78E-04	4.87E-04	5.60E-04	4.20E-04	5.77E-04	7.09E-04	6.59E-04	1.08E-03	6.85E-04	1.05E-03	1.47E-03	3.58e-04	1.05e-04	3.54e-05
³² S	2.62E-02	3.70E-02	4.79E-02	5.74E-02	7.74E-02	1.01E-01	8.55E-02	1.11E-01	1.38E-01	1.07E-01	1.10E-01	1.27E-01	1.22E-01	1.03E-01	1.12e-01	1.12e-01	1.15e-01
³³ S	7.51E-05	1.06E-04	1.42E-04	1.53E-04	2.43E-04	3.14E-04	2.37E-04	3.39E-04	4.21E-04	3.27E-04	5.23E-04	3.65E-04	5.47E-04	6.79E-04	2.39e-04	1.04e-04	4.57e-05
³⁴ S	8.26E-04	1.16E-03	1.57E-03	1.75E-03	2.84E-03	3.73E-03	2.74E-03	4.04E-03	5.02E-03	3.68E-03	6.22E-03	4.22E-03	6.56E-03	8.06E-03	1.86e-03	2.60e-04	7.14e-06
³⁶ S	8.12E-08	1.35E-07	1.65E-07	1.41E-07	2.54E-07	2.57E-07	1.89E-07	2.47E-07	3.05E-07	3.59E-07	5.42E-07	3.23E-07	4.97E-07	7.68E-07	3.86e-08	1.64e-09	1.73e-11
³⁵ Cl	4.29E-05	6.20E-05	8.27E-05	8.37E-05	1.35E-04	1.67E-04	1.27E-04	1.78E-04	2.27E-04	1.89E-04	2.89E-04	2.00E-04	2.98E-04	3.84E-04	9.91e-05	2.64e-05	5.65e-06
³⁷ Cl	7.32E-06	9.62E-06	1.34E-05	1.53E-05	2.26E-05	3.14E-05	2.44E-05	3.51E-05	4.49E-05	3.14E-05	4.66E-05	3.63E-05	5.22E-05	5.75E-05	2.27e-05	9.14e-06	3.52e-06
³⁶ Ar	4.52E-03	6.36E-03	8.03E-03	8.99E-03	1.28E-02	1.61E-02	1.43E-02	1.77E-02	2.17E-02	1.76E-02	1.50E-02	2.08E-02	1.64E-02	1.23E-02	1.85e-02	1.92e-02	2.04e-02
³⁸ Ar	3.77E-04	5.15E-04	7.18E-04	8.01E-04	1.25E-03	1.72E-03	1.29E-03	1.91E-03	2.48E-03	1.69E-03	2.69E-03	1.96E-03	2.98E-03	3.42E-03	8.31e-04	1.19e-04	5.40e-06
⁴⁰ Ar	1.68E-09	2.45E-09	3.13E-09	2.90E-09	4.79E-09	5.27E-09	3.81E-09	5.21E-09	6.60E-09	6.64E-09	1.04E-08	6.29E-09	9.87E-09	1.48E-08	4.66e-10	9.87e-12	5.11e-14
³⁹ K	2.26E-05	2.98E-05	4.12E-05	4.65E-05	6.80E-05	9.52E-05	7.40E-05	1.07E-04	1.39E-04	9.53E-05	1.42E-04	1.10E-04	1.60E-04	1.75E-04	6.25e-05	1.89e-05	3.57e-06
⁴¹ K	1.29E-06	1.65E-06	2.30E-06	2.66E-06	3.80E-06	5.38E-06	4.22E-06	6.08E-06	7.87E-06	5.36E-06	7.81E-06	6.21E-06	8.93E-06	9.65E-06	3.85e-06	1.42e-06	4.92e-07
⁴⁰ Ca	4.05E-03	5.74E-03	7.09E-03	8.82E-03	1.13E-02	1.35E-02	1.24E-02	1.47E-02	1.75E-02	1.50E-02	1.07E-02	1.78E-02	1.10E-02	7.50E-03	1.57e-02	1.66e-02	1.77e-02
⁴² Ca	8.32E-06	1.11E-05	1.55E-05	1.74E-05	2.65E-05	3.69E-05	2.80E-05	4.15E-05	5.44E-05	3.63E-05	5.71E-05	4.22E-05	6.44E-05	7.30E-05	1.67e-05	2.08e-06	8.87e-08
⁴³ Ca	1.63E-08	1.93E-08	2.63E-08	2.92E-08	4.29E-08	5.62E-08	4.37E-08	6.12E-08	7.44E-08	5.57E-08	8.61E-08	6.03E-08	9.21E-08	1.14E-07	2.35e-08	6.22e-09	6.23e-09
⁴⁴ Ca	3.25E-06	4.40E-06	5.24E-06	6.49E-06	8.14E-06	9.14E-06	8.92E-06	1.00E-05	1.11E-05	1.04E-05	6.45E-06	1.19E-05	6.08E-06	4.06E-06	1.08e-05	1.18e-05	1.27e-05
⁴⁶ Ca	1.58E-11	1.99E-11	2.66E-11	2.64E-11	4.01E-11	4.76E-11	7.13E-10	4.85E-11	6.06E-11	5.50E-11	8.60E-11	5.65E-11	8.43E-11	1.24E-10	2.24e-12	5.88e-13	5.82e-13
⁴⁸ Ca	1.97E-15	3.88E-15	7.61E-15	7.56E-15	1.86E-14	5.84E-15	9.97E-11	7.85E-15	3.04E-15	6.17E-15	5.21E-15	8.89E-14	4.52E-15	6.99E-15	5.04e-15	4.85e-15	4.82e-15
⁴⁵ Sc	5.12E-08	6.53E-08	8.56E-08	1.03E-07	1.36E-07	1.83E-07	1.56E-07	2.05E-07	2.51E-07	1.92E-07	2.20E-07	2.48E-07	2.45E-07	2.45E-07	1.43e-07	7.69e-08	3.94e-08
⁴⁶ Ti	4.33E-06	5.72E-06	8.01E-06	9.13E-06	1.33E-05	1.87E-05	1.46E-05	2.11E-05	2.75E-05	1.86E-05	2.72E-05	2.17E-05	3.11E-05	3.34E-05	9.34e-06	1.37e-06	2.19e-07
⁴⁷ Ti	1.80E-07	2.28E-07	3.01E-07	3.58E-07	4.84E-07	6.33E-07	5.44E-07	7.05E-07	8.51E-07	6.53E-07	7.66E-07	7.44E-07	8.46E-07	8.59E-07	3.37e-07	9.30e-08	9.90e-08
⁴⁸ Ti	1.02E-04	1.41E-04	1.67E-04	2.07E-04	2.67E-04	2.85E-04	2.87E-04	3.14E-04	3.36E-04	3.31E-04	1.80E-04	3.78E-04	1.50E-04	9.30E-05	3.43e-04	3.73e-04	3.87e-04
⁴⁹ Ti	8.06E-06	1.07E-05	1.29E-05	1.61E-05	2.07E-05	2.35E-05	2.35E-05	2.59E-05	2.76E-05	2.69E-05	1.72E-05	3.05E-05	1.62E-05	1.03E-05	2.06e-05	1.27e-05	6.83e-06
⁵⁰ Ti	2.48E-08	5.52E-08	1.33E-07	1.44E-07	3.43E-07	1.62E-07	1.02E-04	2.60E-07	6.88E-10	1.61E-07	4.58E-08	1.25E-06	1.19E-09	1.72E-09	2.52e-07	2.47e-07	2.46e-07
⁵⁰ V	8.95E-10	1.21E-09	1.94E-09	2.34E-09	3.70E-09	4.68E-09	3.20E-08	5.56E-09	3.84E-09	5.07E-09	6.16E-09	6.72E-09	6.11E-09	7.52E-09	3.01e-09	2.30e-09	2.28e-09
⁵¹ V	3.41E-05	4.14E-05	5.01E-05	6.18E-05	8.06E-05	9.51E-05	1.51E-04	1.05E-04	1.01E-04	1.09E-04	8.19E-05	1.20E-04	8.09E-05	6.01E-05	7.65e-05	3.99e-05	2.62e-05
⁵⁰ Cr	1.01E-04	1.39E-04	1.84E-04	2.27E-04	3.08E-04	4.06E-04	3.95E-04	4.51E-04	4.63E-04	4.47E-04	4.48E-04	5.05E-04	5.08E-04	4.01E-04	2.53e-04	1.11e-04	8.59e-05
⁵² Cr	3.55E-03	4.06E-03	4.56E-03	5.45E-03	7.23E-03	7.70E-03	1.16E-02	8.57E-03	8.02E-03	8.90E-03	5.62E-03	9.85E-03	4.78E-03	3.94E-03	8.97e-03	9.44e-03	9.64e-03
⁵³ Cr	5.25E-04	5.27E-04	5.91E-04	7.09E-04	9.48E-04	1.12E-03	1.46E-03	1.24E-03	9.98E-04	1.29E-03	1.06E-03	1.36E-03	1.06E-03	9.20E-04	1.02e-03	7.61e-04	6.27e-04
⁵⁴ Cr	9.85E-07	2.06E-06	4.54E-06	5.18E-06	1.08E-05	7.59E-06	1.25E-03	2.61E-07	1.11E-05	8.55E-06	4.94E-06	3.24E-05	3.17E-06	4.06E-06	1.07e-05	1.05e-05	1.05e-05
⁵⁵ Mn	8.74E-03	6.93E-03	6.80E-03	7.61E-03	9.70E-03	1.21E-02	1.39E-02	9.29E-03	1.33E-02	1.39E-02	1.31E-02	1.35E-02	1.31E-02	1.13E-02	1.11e-02	8.73e-03	7.84e-03
⁵⁴ Fe	3.02E-02	3.07E-02	3.84E-02	4.77E-02	6.71E-02	9.00E-02	9.80E-02	9.94E-02	5.70E-02	1.04E-01	1.13E-01	1.0					

Table 3. Nucleosynthetic yields (in solar masses) of select radioactive nuclides at time $t = 100$ s.

	N1	N3	N5	N10	N20	N40	N100H	N100	N100L	N150	N200	N300C	N1600	N1600C	N100.Z0.5	N100.Z0.1	N100.Z0.01
¹⁴ C	2.25E-06	7.64E-06	6.50E-06	2.96E-06	6.39E-06	3.30E-06	3.26E-06	2.47E-06	3.06E-06	1.41E-05	1.02E-05	7.01E-06	7.96E-06	1.44E-05	1.20E-06	1.50E-07	6.57E-10
²² Na	1.90E-09	4.64E-09	4.99E-09	3.03E-09	6.99E-09	5.11E-09	4.67E-09	4.27E-09	5.25E-09	1.17E-08	1.46E-08	8.67E-09	1.18E-08	2.20E-08	4.43E-09	4.60E-09	7.84E-09
²⁶ Al	2.35E-07	5.83E-07	6.13E-07	3.86E-07	8.62E-07	6.57E-07	5.72E-07	5.68E-07	7.16E-07	1.42E-06	1.82E-06	1.08E-06	1.51E-06	2.70E-06	3.73E-07	2.70E-07	9.30E-08
³² Si	6.49E-09	1.61E-08	1.52E-08	8.25E-09	1.78E-08	1.14E-08	9.99E-09	9.47E-09	1.10E-08	3.48E-08	3.04E-08	2.01E-08	2.42E-08	4.38E-08	1.58E-09	1.53E-11	4.58E-15
³² P	1.46E-07	2.55E-07	2.99E-07	2.65E-07	4.80E-07	5.01E-07	3.77E-07	4.96E-07	5.88E-07	6.68E-07	1.03E-06	6.29E-07	9.56E-07	1.42E-06	1.89E-07	2.43E-08	2.02E-10
³³ P	1.00E-07	1.67E-07	2.01E-07	1.93E-07	3.38E-07	3.74E-07	2.74E-07	3.76E-07	4.54E-07	4.44E-07	7.57E-07	4.56E-07	7.17E-07	1.05E-06	1.39E-07	1.33E-08	7.44E-11
³⁵ S	1.78E-07	2.87E-07	3.59E-07	3.08E-07	5.52E-07	5.60E-07	4.16E-07	5.39E-07	6.74E-07	7.86E-07	1.19E-06	7.13E-07	1.09E-06	1.71E-06	8.66E-08	3.58E-09	2.53E-11
³⁶ Cl	2.15E-07	3.24E-07	4.13E-07	3.98E-07	6.72E-07	7.66E-07	5.61E-07	7.77E-07	9.58E-07	9.13E-07	1.48E-06	9.15E-07	1.43E-06	2.07E-06	2.81E-07	3.59E-08	8.47E-10
³⁷ Ar	7.11E-06	9.32E-06	1.30E-05	1.49E-05	2.19E-05	3.06E-05	2.38E-05	3.43E-05	4.39E-05	3.06E-05	4.52E-05	3.54E-05	5.08E-05	5.55E-05	2.25E-05	9.11E-06	3.51E-06
³⁹ Ar	4.13E-09	5.53E-09	7.30E-09	6.96E-09	1.13E-08	1.28E-08	9.56E-09	1.29E-08	1.57E-08	1.58E-08	2.39E-08	1.50E-08	2.28E-08	3.30E-08	2.46E-09	1.19E-10	1.47E-12
⁴⁰ K	1.76E-08	2.39E-08	3.18E-08	3.07E-08	4.89E-08	5.68E-08	4.21E-08	5.81E-08	7.39E-08	6.86E-08	1.06E-07	6.72E-08	1.04E-07	1.48E-07	1.48E-08	1.30E-09	5.80E-11
⁴¹ Ca	1.28E-06	1.65E-06	2.30E-06	2.65E-06	3.80E-06	5.37E-06	4.22E-06	6.07E-06	7.86E-06	5.35E-06	7.79E-06	6.20E-06	8.92E-06	9.63E-06	3.85E-06	1.42E-06	4.92E-07
⁴⁴ Ti	3.24E-06	4.38E-06	5.22E-06	6.47E-06	8.11E-06	9.10E-06	8.88E-06	9.98E-06	1.11E-05	1.03E-05	6.37E-06	1.19E-05	6.00E-06	3.96E-06	1.08E-05	1.18E-05	1.27E-05
⁴⁸ V	1.88E-08	2.47E-08	3.53E-08	4.29E-08	6.23E-08	8.03E-08	7.01E-08	9.12E-08	1.09E-07	8.69E-08	9.80E-08	9.77E-08	1.05E-07	1.10E-07	5.72E-08	3.84E-08	3.01E-08
⁴⁹ V	6.80E-08	9.28E-08	1.31E-07	1.63E-07	2.41E-07	3.15E-07	3.21E-07	3.57E-07	3.93E-07	3.51E-07	3.72E-07	4.00E-07	4.00E-07	4.01E-07	1.95E-07	9.93E-08	6.32E-08
⁴⁸ Cr	1.02E-04	1.41E-04	1.66E-04	2.07E-04	2.67E-04	2.85E-04	2.86E-04	3.14E-04	3.36E-04	3.30E-04	1.79E-04	3.77E-04	1.49E-04	9.24E-05	3.43E-04	3.73E-04	3.87E-04
⁴⁹ Cr	7.99E-06	1.06E-05	1.27E-05	1.59E-05	2.04E-05	2.32E-05	2.29E-05	2.56E-05	2.72E-05	2.66E-05	1.68E-05	3.01E-05	1.58E-05	9.89E-06	2.05E-05	1.26E-05	6.76E-06
⁵¹ Cr	1.39E-06	2.12E-06	3.13E-06	3.89E-06	5.95E-06	8.11E-06	1.13E-05	9.29E-06	7.34E-06	9.13E-06	1.11E-05	1.03E-05	1.34E-05	1.42E-05	5.26E-06	3.53E-06	3.36E-06
⁵¹ Mn	3.27E-05	3.91E-05	4.67E-05	5.76E-05	7.41E-05	8.66E-05	8.61E-05	9.52E-05	9.39E-05	9.91E-05	7.06E-05	1.08E-04	6.74E-05	4.58E-05	7.06E-05	3.58E-05	2.23E-05
⁵² Mn	1.44E-06	1.70E-06	2.10E-06	2.63E-06	3.80E-06	4.57E-06	4.82E-06	5.18E-06	4.77E-06	5.45E-06	4.58E-06	5.87E-06	4.60E-06	3.95E-06	4.61E-06	4.29E-06	4.14E-06
⁵³ Mn	3.06E-05	5.07E-05	7.30E-05	9.66E-05	1.53E-04	2.01E-04	3.78E-04	2.35E-04	8.55E-05	2.48E-04	2.78E-04	2.67E-04	3.56E-04	3.95E-04	1.96E-04	1.77E-04	1.72E-04
⁵⁴ Mn	2.51E-07	5.52E-07	9.36E-07	1.22E-06	2.02E-06	2.44E-06	1.58E-05	3.03E-06	2.60E-07	3.07E-06	3.04E-06	3.86E-06	3.15E-06	4.02E-06	2.84E-06	2.77E-06	2.77E-06
⁵² Fe	3.49E-03	3.94E-03	4.36E-03	5.20E-03	6.80E-03	7.18E-03	7.29E-03	7.93E-03	7.91E-03	8.27E-03	4.98E-03	9.01E-03	4.06E-03	3.03E-03	8.40E-03	8.90E-03	9.10E-03
⁵³ Fe	4.94E-04	4.76E-04	5.17E-04	6.11E-04	7.92E-04	9.12E-04	9.08E-04	1.00E-03	9.12E-04	1.04E-03	7.76E-04	1.08E-03	6.99E-04	5.25E-04	8.17E-04	5.81E-04	4.51E-04
⁵⁵ Fe	1.33E-04	3.40E-04	5.33E-04	7.40E-04	1.20E-03	1.59E-03	2.94E-03	1.86E-03	2.75E-04	2.01E-03	2.37E-03	2.12E-03	3.08E-03	3.29E-03	1.73E-03	1.66E-03	1.66E-03
⁵⁹ Fe	2.93E-10	5.80E-10	1.34E-09	1.47E-09	3.16E-09	1.71E-09	5.10E-07	2.72E-09	1.04E-15	1.81E-09	5.03E-10	1.07E-08	5.75E-13	9.55E-13	2.65E-09	2.60E-09	2.59E-09
⁶⁰ Fe	4.95E-11	1.03E-10	2.45E-10	2.67E-10	6.17E-10	2.60E-10	2.43E-07	4.20E-10	3.64E-18	2.47E-10	4.91E-11	2.35E-09	3.02E-15	5.33E-15	4.07E-10	3.98E-10	3.96E-10
⁵⁵ Co	8.61E-03	6.58E-03	6.26E-03	6.86E-03	8.48E-03	1.05E-02	1.03E-02	1.14E-02	9.01E-03	1.19E-02	1.08E-02	1.13E-02	1.00E-02	8.03E-03	9.33E-03	7.04E-03	6.17E-03
⁵⁶ Co	5.08E-05	4.84E-05	5.45E-05	6.44E-05	8.25E-05	1.08E-04	1.22E-04	1.18E-04	5.43E-05	1.26E-04	1.39E-04	1.19E-04	1.48E-04	1.21E-04	1.07E-04	9.92E-05	9.66E-05
⁵⁷ Co	5.71E-05	1.58E-04	2.50E-04	3.52E-04	5.69E-04	7.44E-04	1.36E-03	8.70E-04	6.54E-05	9.52E-04	1.11E-03	9.92E-04	1.42E-03	1.50E-03	8.43E-04	8.28E-04	8.25E-04
⁵⁸ Co	3.11E-07	7.94E-07	1.30E-06	1.79E-06	2.88E-06	3.63E-06	1.07E-05	4.35E-06	1.23E-07	4.72E-06	5.04E-06	5.14E-06	6.08E-06	7.29E-06	4.27E-06	4.22E-06	4.21E-06
⁶⁰ Co	2.01E-09	3.77E-09	8.36E-09	9.40E-09	1.78E-08	1.36E-08	8.78E-07	2.03E-08	6.97E-13	1.59E-08	6.87E-09	4.97E-08	2.04E-10	3.00E-10	1.99E-08	1.96E-08	1.96E-08
⁵⁶ Ni	1.11E-00	1.04E-00	9.74E-01	9.39E-01	7.78E-01	6.55E-01	6.94E-01	6.04E-01	5.32E-01	5.66E-01	4.15E-01	5.12E-01	3.64E-01	3.22E-01	6.29E-01	6.49E-01	6.55E-01
⁵⁷ Ni	3.36E-02	3.04E-02	2.89E-02	2.78E-02	2.25E-02	1.96E-02	2.06E-02	1.79E-02	1.42E-02	1.69E-02	1.42E-02	1.45E-02	1.31E-02	1.11E-02	1.57E-02	1.33E-02	1.19E-02
⁵⁹ Ni	8.22E-05	1.32E-04	1.78E-04	2.22E-04	3.01E-04	3.57E-04	5.67E-04	3.93E-04	5.78E-05	4.22E-04	4.80E-04	4.23E-04	5.82E-04	5.77E-04	3.80E-04	3.63E-04	4.14E-04
⁶³ Ni	1.85E-09	3.43E-09	7.79E-09	8.72E-09	1.74E-08	1.13E-08	1.38E-06	1.76E-08	1.58E-14	1.27E-08	4.26E-09	5.31E-08	1.85E-11	2.92E-11	1.72E-08	1.69E-08	1.68E-08
⁶² Zn	6.48E-04	7.18E-04	7.80E-04	7.72E-04	6.86E-04	4.74E-04	5.25E-04	3.22E-04	2.45E-04	2.31E-04	9.92E-05	1.34E-04	9.39E-05	9.86E-05	2.24E-04	7.89E-05	5.01E-05
⁶² Zn	3.56E-10	4.88E-10	6.69E-10	7.18E-10	8.76E-10	8.30E-10	1.62E-09	7.35E-10	4.09E-10	6.35E-10	4.11E-10	5.23E-10	3.95E-10	5.08E-10	8.46E-10	9.95E-10	1.11E-09
⁶³ Ge	5.98E-08	6.80E-08	8.19E-08	8.30E-08	8.57E-08	7.07E-08	7.22E-08	5.29E-08	4.32E-08	3.99E-08	1.66E-08	2.07E-08	1.69E-08	2.03E-08	6.64E-08	8.45E-08	9.79E-08
⁶⁸ Ge	8.91E-10	9.19E-10	1.06E-09	1.07E-09	1.03E-09	8.30E-10	8.90E-10	6.33E-10	5.26E-10	5.05E-10	2.40E-10	2.84E-10	2.29E-10	2.53E-10	2.81E-10	8.32E-11	6.38E-11

EXC 153. FKR, MF and SAS acknowledge travel support by the DAAD/Go8 German-Australian exchange program.

REFERENCES

- Arnett W. D., 1969, APSS, 5, 180
- Blinnikov S. I., Khokhlov A. M., 1986, Soviet Astronomy Letters, 12, 131
- Blondin S., Kasen D., Röpke F. K., Kirshner R. P., Mandel K. S., 2011, MNRAS, 417, 1280
- Bloom J. S. et al., 2012, ApJL, 744, L17
- Brachwitz F. et al., 2000, ApJ, 536, 934
- Bravo E., García-Senz D., 2008, A&A, 478, 843
- Bravo E., García-Senz D., 2009, ApJ, 695, 1244
- Bravo E., García-Senz D., Cabezón R. M., Domínguez I., 2009, ApJ, 695, 1257
- Chan K.-W., Lingenfelter R. E., 1993, ApJ, 405, 614
- Chomiuk L. et al., 2012, ApJ, 750, 164
- Clayton D., 2003, Handbook of Isotopes in the Cosmos
- Colella P., Woodward P. R., 1984, Journal of Computational Physics, 54, 174
- Dilday B. et al., 2012, ArXiv e-prints
- Dursi L. J., Timmes F. X., 2006, ApJ, 641, 1071
- Fink M., Hillebrandt W., Röpke F. K., 2007, A&A, 476, 1133
- Fink M., Röpke F. K., Hillebrandt W., Seitenzahl I. R., Sim S. A., Kromer M., 2010, A&A, 514, A53
- Fryxell B. A., Müller E., Arnett W. D., 1989, Hydrodynamics and nuclear burning. MPA Green Report 449, Max-Planck-Institut für Astrophysik, Garching
- Gamezo V. N., Khokhlov A. M., Oran E. S., 2005, ApJ, 623, 337
- Gamezo V. N., Wheeler J. C., Khokhlov A. M., Oran E. S., 1999, ApJ, 512, 827
- García-Senz D., Woosley S. E., 1995, ApJ, 454, 895
- Gilfanov M., Bogdán Á., 2010, Nature, 463, 924
- Han Z., Podsiadlowski P., 2004, MNRAS, 350, 1301
- Höflich P., Gerardy C. L., Nomoto K., Motohara K., Fesen R. A., Maeda K., Ohkubo T., Tominaga N., 2004, ApJ, 617, 1258
- Höflich P., Khokhlov A., 1996, ApJ, 457, 500
- Höflich P., Stein J., 2002, ApJ, 568, 779
- Iapichino L., Brüggén M., Hillebrandt W., Niemeyer J. C., 2006, A&A, 450, 655
- Iwamoto K., Brachwitz F., Nomoto K., Kishimoto N., Umeda H., Hix W. R., Thielemann F.-K., 1999, ApJS, 125, 439
- Jordan, IV G. C., Fisher R. T., Townsley D. M., Calder A. C., Graziani C., Asida S., Lamb D. Q., Truran J. W., 2008, ApJ, 681, 1448
- Jordan, IV G. C. et al., 2012, ArXiv e-prints

- Kasen D., Röpke F. K., Woosley S. E., 2009, *Nature*, 460, 869
- Kasen D., Thomas R. C., Nugent P., 2006, *ApJ*, 651, 366
- Kerstein A. R., 1988, *Combust. Sci. Technol.*, 60, 441
- Khokhlov A. M., 1989, *MNRAS*, 239, 785
- Khokhlov A. M., 1991a, *A&A*, 245, 114
- Khokhlov A. M., 1991b, *A&A*, 246, 383
- Khokhlov A. M., 1991c, *A&A*, 245, L25
- Khokhlov A. M., 1995, *ApJ*, 449, 695
- Khokhlov A. M., Oran E. S., Wheeler J. C., 1997, *ApJ*, 478, 678
- Kobayashi C., Nomoto K., 2009, *ApJ*, 707, 1466
- Kozma C., Fransson C., Hillebrandt W., Travaglio C., Sollerman J., Reinecke M., Röpke F. K., Spyromilio J., 2005, *A&A*, 437, 983
- Kromer M., Sim S. A., Fink M., Röpke F. K., Seitenzahl I. R., Hillebrandt W., 2010, *ApJ*, 719, 1067
- Krueger B. K., Jackson A. P., Townsley D. M., Calder A. C., Brown E. F., Timmes F. X., 2010, *ApJL*, 719, L5
- Kuhlen M., Woosley S. E., Glatzmaier G. A., 2006, *ApJ*, 640, 407
- Lisewski A. M., Hillebrandt W., Woosley S. E., 2000, *ApJ*, 538, 831
- Livne E., 1990, *ApJL*, 354, L53
- Livne E., Glasner A. S., 1990, *ApJ*, 361, 244
- Lodders K., 2003, *ApJ*, 591, 1220
- Maeda K. et al., 2010a, *Nature*, 466, 82
- Maeda K., Röpke F. K., Fink M., Hillebrandt W., Travaglio C., Thielemann F., 2010b, *ApJ*, 712, 624
- Maier A., Niemeyer J. C., 2006, *A&A*, 451, 207
- Mazzali P. A., Röpke F. K., Benetti S., Hillebrandt W., 2007, *Science*, 315, 825
- Meakin C. A., Seitenzahl I., Townsley D., Jordan G. C., Truran J., Lamb D., 2009, *ApJ*, 693, 1188
- Mennekens N., Vanbeveren D., De Greve J. P., De Donder E., 2010, *ArXiv e-prints*
- Nelemans G., Toonen S., Bours M., 2012, *ArXiv e-prints*
- Niemeyer J. C., Woosley S. E., 1997, *ApJ*, 475, 740
- Nomoto K., Thielemann F.-K., Yokoi K., 1984, *ApJ*, 286, 644
- Nonaka A., Aspden A. J., Zingale M., Almgren A. S., Bell J. B., Woosley S. E., 2012, *ApJ*, 745, 73
- Nugent P., Baron E., Branch D., Fisher A., Hauschildt P. H., 1997, *ApJ*, 485, 812
- Osher S., Sethian J. A., 1988, *Journal of Computational Physics*, 79, 12
- Pakmor R., Edelmann P., Röpke F. K., Hillebrandt W., 2011, *Stellar gadget*, in preparation
- Pakmor R., Kromer M., Röpke F. K., Sim S. A., Ruiter A. J., Hillebrandt W., 2010, *Nature*, 463, 61
- Pakmor R., Kromer M., Taubenberger S., Sim S. A., Röpke F. K., Hillebrandt W., 2012, *ApJL*, 747, L10
- Patat F. et al., 2007, *Science*, 317, 924
- Perlmutter S. et al., 1999, *ApJ*, 517, 565
- Phillips M. M., 1993, *ApJL*, 413, L105
- Phillips M. M., Lira P., Suntzeff N. B., Schommer R. A., Hamuy M., Maza J., 1999, *AJ*, 118, 1766
- Prantzos N. et al., 2011, *Reviews of Modern Physics*, 83, 1001
- Prialnik D., Kovetz A., 1995, *ApJ*, 445, 789
- Reinecke M., Hillebrandt W., Niemeyer J. C., Klein R., Gröbl A., 1999, *A&A*, 347, 724
- Riess A. G. et al., 1998, *AJ*, 116, 1009
- Röpke F. K., 2005, *A&A*, 432, 969
- Röpke F. K., 2007, *ApJ*, 668, 1103
- Röpke F. K., Gieseler M., Reinecke M., Travaglio C., Hillebrandt W., 2006a, *A&A*, 453, 203
- Röpke F. K., Hillebrandt W., Niemeyer J. C., Woosley S. E., 2006b, *A&A*, 448, 1
- Röpke F. K., Hillebrandt W., Schmidt W., Niemeyer J. C., Blinnikov S. I., Mazzali P. A., 2007a, *ApJ*, 668, 1132
- Röpke F. K. et al., 2012, *ApJL*, 750, L19
- Röpke F. K., Niemeyer J. C., 2007, *A&A*, 464, 683
- Röpke F. K., Woosley S. E., Hillebrandt W., 2007b, *ApJ*, 660, 1344
- Ruiter A. J., Belczynski K., Fryer C., 2009, *ApJ*, 699, 2026
- Ruiter A. J., Belczynski K., Sim S. A., Hillebrandt W., Fryer C. L., Fink M., Kromer M., 2011, *MNRAS*, 1282
- Scannapieco C., Tissera P. B., White S. D. M., Springel V., 2008, *MNRAS*, 389, 1137
- Schmidt B. P. et al., 1998, *ApJ*, 507, 46
- Schmidt W., Niemeyer J. C., Hillebrandt W., 2006a, *A&A*, 450, 265
- Schmidt W., Niemeyer J. C., Hillebrandt W., Röpke F. K., 2006b, *A&A*, 450, 283
- Seitenzahl I., 2011, *Progress in Particle and Nuclear Physics*, 66, 329, particle and Nuclear Astrophysics, International Workshop on Nuclear Physics, 32nd Course
- Seitenzahl I. R., Ciaraldi-Schoolmann F., Röpke F. K., 2011, *MNRAS*, 414, 2709
- Seitenzahl I. R., Meakin C. A., Lamb D. Q., Truran J. W., 2009a, *ApJ*, 700, 642
- Seitenzahl I. R., Meakin C. A., Townsley D. M., Lamb D. Q., Truran J. W., 2009b, *ApJ*, 696, 515
- Seitenzahl I. R., Röpke F. K., Fink M., Pakmor R., 2010, *MNRAS*, 407, 2297
- Seitenzahl I. R., Taubenberger S., Sim S. A., 2009c, *MNRAS*, 400, 531
- Seitenzahl I. R., Townsley D. M., Peng F., Truran J. W., 2009d, *Atomic Data and Nuclear Data Tables*, 95, 96
- Sim S. A., 2007, *MNRAS*, 375, 154
- Sim S. A., Röpke F. K., Hillebrandt W., Kromer M., Pakmor R., Fink M., Ruiter A. J., Seitenzahl I. R., 2010, *ApJL*, 714, L52
- Smiljanovski V., Moser V., Klein R., 1997, *Combustion Theory Modelling*, 1, 183
- Sreenivasan K. R., 1991, *Annual Review of Fluid Mechanics*, 23, 539
- Stehle M., Mazzali P. A., Benetti S., Hillebrandt W., 2005, *MNRAS*, 360, 1231
- Sternberg A. et al., 2011, *Science*, 333, 856
- Stritzinger M., Mazzali P. A., Sollerman J., Benetti S., 2006, *A&A*, 460, 793
- Timmes F. X., Brown E. F., Truran J. W., 2003, *ApJL*, 590, L83
- Timmes F. X., Woosley S. E., 1992, *ApJ*, 396, 649
- Timmes F. X., Woosley S. E., Weaver T. A., 1995, *ApJS*, 98, 617
- Townsley D. M., Calder A. C., Asida S. M., Seitenzahl I. R., Peng F., Vladimirova N., Lamb D. Q., Truran J. W., 2007, *ApJ*, 668, 1118
- Travaglio C., Hillebrandt W., Reinecke M., 2005, *A&A*, 443, 1007
- Travaglio C., Hillebrandt W., Reinecke M., Thielemann F.-K., 2004, *A&A*, 425, 1029
- Travaglio C., Röpke F. K., Gallino R., Hillebrandt W., 2011, *ApJ*, 739, 93
- van der Sluys M., Politano M., Taam R. E., 2010, 1314, 13
- Wang B., Li X.-D., Han Z.-W., 2010, *MNRAS*, 401, 2729
- Wang L., Wheeler J. C., 2008, *ARA&A*, 46, 433
- Woosley S. E., 2007, *ApJ*, 668, 1109
- Woosley S. E., Kerstein A. R., Aspden A. J., 2011, *ApJ*, 734, 37

- Woosley S. E., Kerstein A. R., Sankaran V., Aspden A. J., Röpke F. K., 2009, *ApJ*, 704, 255
- Woosley S. E., Weaver T. A., 1994, in *Les Houches Session LIV: Supernovae*, Bludman S. A., Mochkovitch R., Zinn-Justin J., eds., North-Holland, Amsterdam, pp. 63–154
- Woosley S. E., Wunsch S., Kuhlen M., 2004, *ApJ*, 607, 921
- Zel'dovich Y. B., Librovich V. B., Makhviladze G. M., Sivashinskii G. I., 1970, *Journal of Applied Mechanics and Technical Physics*, 11, 264
- Zingale M., Almgren A. S., Bell J. B., Nonaka A., Woosley S. E., 2009, *ApJ*, 704, 196